VASP phase separation with priming proteins of fast endophilin mediated endocytosis modulates actin polymerization

Karthik B. Narayan[1], Honey Priya James[1], Jonathan Cope[2], Samsuzzoha Mondal[1], Laura Baeyens[1], Francesco Milano[1], Jason Zheng[1], Matthias Krause[2], Tobias Baumgart[1]*

[1] Department of Chemistry, University of Pennsylvania, Philadelphia, 19104, USA
[2] Randall Centre for Cell & Molecular Biophysics, School of Basic & Medical Biosciences, King's College London, New Hunt's House, Guy's Campus, London, SE1 1UL, UK
* To whom correspondence may be addressed: baumgart@sas.upenn.edu

Abstract

Actin polymerization is essential in several clathrin-independent endocytic pathways including fast endophilin mediated endocytosis (FEME), however the actin machinery involved in FEME has been elusive. Here, we show that the actin polymerase VASP colocalizes and interacts directly with the FEME priming complex. We identify endophilin (EDP) as a VASP binding partner and establish novel non-canonical interactions between EDP and the EVH1 and EVH2 domains of VASP. The major FEME regulators EDP and lamellipodin (LPD) interact multivalently with VASP undergoing liquid-liquid phase separation both in solution and on lipid membranes. We show that priming complex mimicking condensates localise actin polymerization, with LPD-VASP promoting and EDP antagonising actin assembly, suggesting a novel role for EDP during the priming step of FEME. Finally, we show that LPD and EDP recruits and clusters VASP on lipid membranes mimicking the plasma membrane's inner leaflet to locally assemble actin filaments. Our results support a model where actin polymerization in FEME is spatiotemporally initiated by the depletion of EDP, mediated by receptor activation.

Teaser

Liquid-like condensates formed by actin polymerases and endocytic proteins, localise and regulate actin polymerization.

Introduction

Endocytosis mediates the internalization of transmembrane proteins and nutrients that are too large to diffuse through the plasma membrane. Numerous distinct endocytic pathways exist and can be categorized based on their dependence on clathrin, a membrane scaffolding protein, into clathrin mediated endocytosis (CME) and clathrin independent endocytosis (CIE). While CME is the prominent form of endocytosis in eukaryotes[1], CIE routes function in parallel to internalize specific cargo[2]. CIE pathways like FEME are responsible for the uptake of activated receptors at the leading edge of cells to support migration[3]. In addition to being used for the exclusive internalization of certain receptors including β1-Adrenergic receptor (β1AR) and of the Epidermal Growth Factor Receptor (EGF receptor) when stimulated with high concentrations of EGF, it also acts as a pathway for rapid cargo uptake[3]. The successful uptake of cargo in both CME

and CIE depends on the precise execution of multiple steps, which include the generation of membrane invaginations[1,2,4,5] and the local polymerization of actin[6-8].

Actin polymerization is an indispensable step for the successful internalization of cargo in most CIE pathways including FEME[3], but the identity, recruitment and activation of the polymerization machinery and its interplay with membrane curvature generators is limited. Actin networks formed in-cellulo are a result of multiple polymerization machineries working in unison, often including nucleation promotion factors (NPFs) like N-WASP[9], that activate the Arp2/3 complex and allow for the formation of branched actin networks, formins[10] and Ena/VASP[11] proteins that elongate actin filaments[12]. Interestingly, multiple studies have established a direct link between the membrane remodelling BAR (Bin, amphiphysin and Rvs) domain containing proteins and cytoskeletal regulators[13-17], prompting a need to understand the interplay between actin machineries[11,18] and membrane curvature generators[8,13] in recently discovered pathways like FEME.

In FEME, the BAR domain containing proteins EDP A1 and A2 (referred to as EDP throughout the text) are recruited by LPD, an adaptor protein found at the leading edge, through interactions between EDP's SH3 domain and the ten proline rich motifs (PRMs) found in LPD's highly disordered C-terminal tail[14]. EDP A1-2 exist as homodimers that dimerize via their BAR domain and contain an intrinsically disordered linker that separates the SH3 domain from the BAR domain (Fig 1I). Through multivalent interactions, LPD and EDP are enriched in transient protein patches on the plasma membrane primed for endocytosis termed FEME priming patches[3,19,20]. Along with its role in the formation of endocytic patches, EDP recruits dynamin, a downstream endocytic protein involved in membrane scission[21,22]. LPD recruits Ena/VASP proteins to the leading edge of cells[23,24] and to clathrin-coated pits to support membrane scission[14]. We previously determined that LPD also recruits EDP A1-2[14], collectively showing that LPD via EDP A1-2 and Ena/VASP proteins promote CME of the EGFR. This prompted us to explore in this study the possibility that Ena/VASP functions with LPD and both EDP A1 and A2 in FEME.

The Ena/VASP protein family, Mena, VASP, EVL in vertebrates, are homotetramers with each monomer comprised of an EVH1 and EVH2 (Ena/VASP Homology 1 or 2) domain connected by a disordered linker (Fig 1I). This proline rich linker harbours profilin and profilin-actin binding sites[25], and enables interactions with SH3 domain containing proteins like c-Abl[26] and IRSp53[15]. Ena/VASP proteins are recruited to the leading edge by the binding of their EVH1 domains to the seven VASP binding motifs found in LPD's C-terminal tail (Fig 1I). The EVH2 domain engages with G and F actin enabling the speed up of actin filament elongation by temporarily preventing capping of actin filament barbed ends by capping protein and by the recruitment of polymerisation competent G-actin[11]. The need for profilin for VASP mediated actin polymerization has been inconclusive, with recent observations showing that Ena/VASP proteins effectively assemble pure and profilin bound actin[27]. Cellularly, the enrichment of the Ena/VASP proteins at the leading edge is often accompanied by formation of filopodia[15] or development of lamellipodial fronts[23], conferring an important role for Ena/VASP proteins in cell migration. Amongst the Ena/VASP proteins, VASP has been studied in most detail.

Multivalency is a key feature of the interactions between VASP and its binding partners including LPD. Biomolecules that interact multivalently can result in the formation of liquid-like condensates by a phenomenon called liquid-liquid phase separation (LLPS)[20,28,29]. LLPS has been demonstrated to play a critical role in the organization and function of proteins in-cellulo as the liquid-like condensates offer a platform to locally enrich proteins by specific sequestration, and to regulate reaction kinetics[30-32]. Interestingly several actin and microtubule regulators[29,33,34] including VASP[35] undergo LLPS that can drive the rapid polymerization of cytoskeletal proteins. Furthermore, recent contributions by us and others have shown that endocytic proteins[20,36-40] can form liquid like condensates at various stages of endocytosis. Our understanding of the function of LLPS in endocytosis is developing, and likely is important for the generation of membrane curvature and the regulation of actin polymerization.

FEME is a rapid endocytic pathway[3] which requires precise execution of tightly orchestrated events for successful internalization. One important but poorly resolved step in the pathway is the rapid, local polymerization of actin. Towards understanding this step better, we investigate the role of the Ena/VASP family protein VASP and show that VASP is found on FEME priming patches. In-vitro, VASP undergoes LLPS with EDP and LPD. We also show that LPD-VASP condensates promotes localised actin polymerization in both a solution and membrane environment. The presence of EDP suppresses LPD-VASP mediated actin polymerization, suggesting that initially EDP limits LPD-VASP mediated actin polymerisation during the priming step of FEME. Finally, we test the ability of the LPD-VASP-EDP A1 complex to induce actin polymerisation in a membrane context. We find that VASP can be recruited to lipid membranes that resemble the inner leaflet of the plasma membrane by either LPD or EDP-A1, allowing for membrane proximal actin polymerization. This study expands our understanding of the actin machinery and their interplay with curvature generating proteins in FEME.

Results

VASP binds EDP and they colocalize at FEME priming sites

FEME priming patches are generated by the recruitment of endocytic proteins like EDP-A1-2 by LPD at the leading edge[19]. The local polymerization of actin is essential for the formation of these priming patches[3], however the actin polymerases involved in the pathway are still unknown. We wondered whether VASP, due to its known interaction with LPD, could be involved in the endocytic pathway. Using BSC1 cells, which have been documented to exhibit robust FEME[41], we assessed the colocalization of VASP with FEME priming patches at the leading edge of the cells by co-immunostaining the cells for EDP-A2 and VASP. Interestingly, endogenous VASP and Mena (another member of the Ena/VASP family) showed strong colocalization with EDP-A2 at FEME priming patches but not with EDP-A2 on FEME carriers distal from the membrane (Fig 1A). This result suggests a possible role for VASP in the early stages of FEME, namely the generation of priming patches and/or during membrane invagination and scission.

Next, we set out to understand the mechanism of the recruitment of VASP to the FEME priming patches. It is known that VASP interacts with SH3 domain containing proteins like IRSp53 and c-Abl[15,26,42]. Therefore, we wondered whether VASP-EDP (going forward all in-vitro studies are performed with EDP A1 and will be referred to as EDP) binding could act complementarily to VASP's well-known interaction with LPD, providing multiple routes of localization to FEME priming patches. To test this idea, we performed a pull-down of mScarlet-VASP containing HeLa cell lysate with GST tagged EDP and EDP-ΔSH3 as baits. Consistent with our prediction, we observed significant binding of VASP to EDP in an SH3 domain dependent manner (Fig 1B, Supplementary Fig. 1). As VASP contains numerous sites for post-translation modifications (PTM) including acetylation, glycosylation and phosphorylation, we wondered whether VASP's native PTMs were required for its interaction with EDP. Additionally, as the cell lysate used in the pull-down contains proteins like LPD that could facilitate interactions of VASP and EDP by acting as a bridging protein, we decided to verify the direct binding of VASP to EDP. We recombinantly expressed and purified VASP from E. coli, which lacks most eukaryotic post-translational machineries including kinases specific for serine, threonine and tyrosine residues[43,44]. When used in place of mScarlet-VASP expressing cell lysate, we observed the pull-down of fluorescently labelled, purified VASP by full length EDP, but not by EDP-ΔSH3, showing that VASP interacts directly with EDP, and is mediated by EDP's SH3 domain.

To identify the specific regions of VASP that interact with EDP's SH3 domain, we generated cell lysate from HeLa cells expressing mScarlet tagged domains of VASP (EVH1, EVH2 and linker) and used them for the pull-down assay as described earlier. Unexpectedly, VASP's proline-rich linker which harbours SH3 binding sites, did not get pulled down by EDP (Fig 1B). Interestingly, we observed binding of both the EVH1 and EVH2 domains of VASP to EDP's SH3 domain (Fig 1B, 1C). This was surprising as conventionally the EVH1 domain specifically binds the 'FPPPP' motifs found in proteins like LPD, and the EVH2 domain is an F- and G-actin binding domain. This discovery opens the possibility of increased multivalency between VASP and EDP-A1-2 involving both the EVH1 and the EVH2 domains of tetrameric VASP and the SH3 domains of dimeric EDP-A1-2.

EDP and VASP co-exist in liquid-like condensates in vitro

FEME priming patches are likely phase separated domains formed as a result of multivalent interactions between essential endocytic initiators including EDP and LPD[20]. As VASP and EDP are known drivers of phase separation[20,35], coupled with our finding that VASP and EDP are multivalent binding partners, we wondered if VASP and EDP interactions could result in phase separation. Using bacterially purified full length VASP and EDP, we investigated the phase separation of the proteins in bulk mixtures. We noticed that only in the presence of a molecular crowder (3% PEG), droplets emerged in solution (Fig 1D), with both proteins enriched within the condensates (Fig 1E). At the concentrations used, VASP[35] has been previously reported to undergo LLPS in the presence of 3% PEG, however EDP does not[20]. The observation of strong endophilin

partitioning into the condensates suggests that specific VASP-EDP interactions enable EDP to co-exist with VASP in liquid-like condensates in the bulk.

We next assessed the mobility of the proteins in the condensates using fluorescence recovery after photobleaching (FRAP). We observed incomplete recovery of fluorescence after bleaching suggesting that the proteins in the condensates behaved partially liquid-like. EDP condensates formed in the presence of PEG have been reported to show partial photorecovery[20], while VASP condensates formed under similar conditions are very liquid like[35]. This suggests that the diffusion of VASP and EDP in a co-phase separated condensate state is strongly influenced by EDP's tendency to diffuse slowly in PEG-induced condensates.

In our recent contribution, we showed that multivalent LPD-EDP interactions result in LLPS, likely promoting the formation of FEME priming patches. Considering the colocalization of EDP, VASP and LPD on FEME priming patches, we were curious to understand how VASP affected the capacity of EDP and the C-terminal tail of LPD between residues 850-1250 (This construct will be referred to as $LPD^{850-1250}$ henceforth in the study.) to phase separate. When introduced in the bulk, VASP co-phase separated with $LPD^{850-1250}$ and EDP forming condensates in the absence of a molecular crowder, and exhibited liquid-like characteristics (Fig 1G, 1H). We observed $LPD^{850-1250}$ to form speckles within the condensate suggesting that the protein might be forming small clusters. EDP A2 was tested in place of A1 and similar results were obtained (data not shown). As VASP-LPD interactions are multivalent in nature and are implicated in multiple cellular pathways including FEME, we investigated their ability to undergo and utilize LLPS to drive actin polymerization.

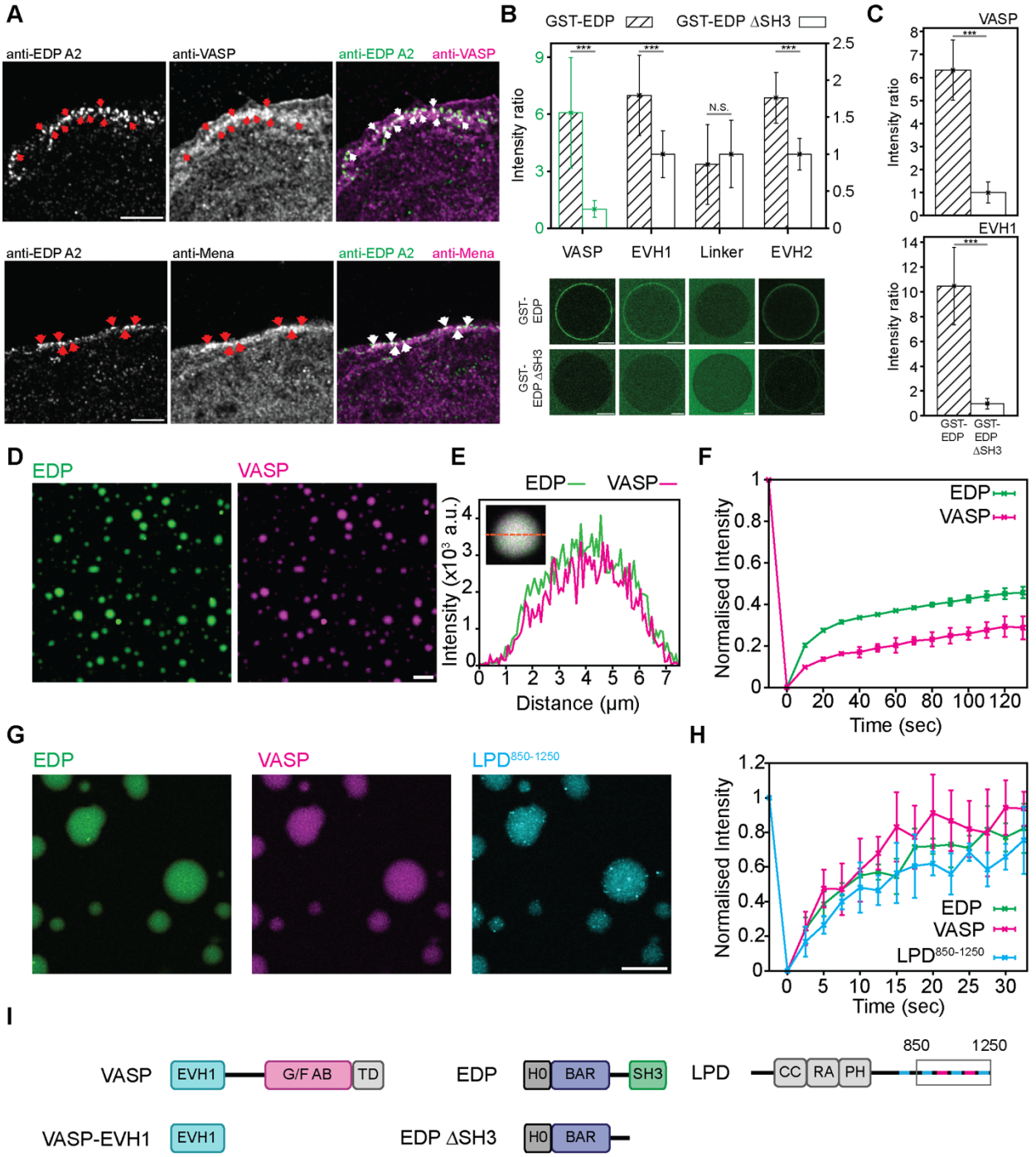

Figure 1: EDP and VASP are multivalent binding partners that undergo LLPS.

A) Endogenous colocalization of the Ena/VASP proteins, VASP and Mena with EDP-A2 at the leading edge of resting BSC1 cells. Scale bar 5 µm.

B) Top Fluorescence intensity of mScarlet VASP and its truncates pulled down on Glutathione Sepharose 4B beads coupled with either 25 µM of GST-EDP or GST-EDP ΔSH3, normalized by mScarlet intensity on GST-EDP ΔSH3 beads. Two different axes are shown. The left-hand axis (shown in green) is applicable to the VASP ratio (data highlighted in green) and the right-hand side axis (shown in black) is applicable to the EVH1, EVH2 and the linker pull-down ratios highlighted in black. Lysate prepared from HeLa cells expressing mScarlet VASP (and truncates) was incubated with GST tagged protein coupled beads for 30

minutes. Beads were washed and imaged. N > 10 for all experiments. **Bottom** Representative fluorescence images of beads tagged with either GST-EDP or GST-EDP ΔSH3 incubated with the respective lysates showing significant binding of VASP, EVH1 and EVH2 to GST-EDP. Scale Bar 20 µm.
C) Pull-down intensity ratio similar to **B** performed using purified proteins. 5 µM VASP or EVH1 domain of VASP with 250 nM Alexa 594 labelled VASP or EVH1 respectively. Proteins were incubated with GST-EDP or GST-EDP ΔSH3 coupled Glutathione Sepharose 4B beads for 30 minutes, washed and imaged. N > 10 for all experiments.
D) Phase separated droplets formed by 25 µM each EDP and VASP with 250 nM Alexa 488 and 594 labelled proteins respectively, in the presence of 3% PEG. Scale bar 10 µm.
E) Line intensity profile along red dashed line shown in inset image. Droplet generated under conditions described in **D**.
F) Normalized FRAP profile of VASP and EDP in condensates described in **D**. The error bars represent the standard deviation of 3 independent samples.
G) Condensates created by the mixture of 25 µM each of EDP, VASP and $LPD^{850-1250}$ doped with 500 nM of labelled protein (EDP-Alexa 488, VASP-Alexa 594 and $LPD^{850-1250}$ Alexa 647). Scale bar 10 µm.
H) Normalized FRAP intensity curve of EDP, VASP and $LPD^{850-1250}$ for conditions described in **G**. The error bars are the standard deviation of the intensities of 3 independent experiments.
I) Schematic depicting the domains of Top row: LPD (In box $LPD^{850-1250}$), VASP and EDP, and Bottom row: EVH1 domain of VASP and EDPΔSH3. Blue and magenta strips in LPD's C terminal tail represent the SH3 and EVH1 binding sites.
Analysis: unpaired student t test was performed with *** and ** corresponding to a p value of < 0.005 and 0.05

VASP and $LPD^{850-1250}$ undergo bulk and membrane associated phase separation in-vitro

LPD's PH domain binds PI(3,4)P2 lipids that are enriched at the leading edge of cells[23]. Downstream binding partners of LPD are subsequently recruited to initiate processes like endocytosis, and the generation of filopodia and lamellipodia[3,14,23,24,45]. VASP, a LPD binding partner, is one of the key proteins involved in actin polymerization required for cell migration[11,23,46]. VASP's N terminal EVH1 domain binds multiple poly proline stretches found on LPD's C terminal tail[23]. Both LPD and VASP possess coiled-coil motifs in their sequences allowing for their formation of homo-dimers and tetramers respectively. Motivated by prior observations of transient clusters of VASP and LPD at filopodial tips[47], and of in-vitro VASP condensates[20,35], we asked whether the multivalent interactions between LPD and VASP could result in the formation of liquid like condensates.

Utilizing $LPD^{850-1250}$ which contains all seven EVH1 binding sites[12,45], the phase separation of bacterially purified $LPD^{850-1250}$ and VASP was studied both in solution and on planar lipid bilayers (SLB), which are a commonly used model membrane system that mimics bio-membranes[20,28,29,48-50].

In solution, interactions between $LPD^{850-1250}$ and VASP resulted in the formation of condensates enriched in both $LPD^{850-1250}$ and VASP (Fig 2A, 2C). The condensates exhibited classic liquid-like characteristics and showed recovery of fluorescence upon photobleaching (Fig 2A). We wondered whether, similar to VASP[35], electrostatics played a critical role in the formation $LPD^{850-1250}$-VASP condensates. To test this hypothesis, we attempted to generate condensates at increased buffer ionic strengths. We observed a loss of condensate formation (as confirmed by light microscopy), at higher salt

concentration (500 and 1000 mM NaCl) in comparison to the control (120 mM NaCl), indicating that $LPD^{850-1250}$-VASP phase separation is facilitated by electrostatic attraction (Supplementary Fig. 2). To assess the role of multivalency conferred by VASP's tetramerization domain in the formation of protein condensates with $LPD^{850-1250}$, we generated a monomeric VASP truncate (lacking the tetramerization domain, VASP-ΔTD). Consistent with indispensable role of high valency interactions, the ΔTD truncate was unable to phase separate with $LPD^{850-1250}$ (Fig 2D). To further confirm that multivalent interactions between $LPD^{850-1250}$ and VASP result in the formation of phase separated condensates, we introduced the monomeric EVH1 (LPD binding domain of VASP) in excess as a competitor with $LPD^{850-1250}$ and VASP in solution. Consistent with previous observations[28], the introduction of the monomer resulted in a suppression of phase separation, resulting in a significant reduction in the abundance and size of the condensates formed (Supplementary Fig. 3). Together, these results show that multivalent $LPD^{850-1250}$-VASP interactions in the bulk result in liquid-like phase separation.

We next sought to recapitulate the interactions of $LPD^{850-1250}$ and VASP in a membrane proximal environment. The $LPD^{850-1250}$ construct was designed to have a C-terminal poly-histidine tag that was used to tether the protein to Ni-NTA functionalized lipids. VASP truncates were incubated with bilayers coupled with $LPD^{850-1250}$ and imaged after 30 minutes. In keeping with the bulk experiments, full length VASP formed membrane bound clusters with $LPD^{850-1250}$ (Fig 2B, 2C), whereas VASP-ΔTD truncate did not result in domain formation (Fig 2E). We performed an auto-correlation analysis to quantify the extent of $LPD^{850-1250}$'s clustering on the lipid bilayer in the presence of VASP and VASPΔTD. An increase in the correlation length (indicative of clustering) is only seen in the presence of $LPD^{850-1250}$ and VASP, but not with ΔTD (Fig 2F). We suspect that the negative correlation seen in the $LPD^{850-1250}$+VASP (purple curve in Fig. 2F around 1 μm) is due to the local depletion of $LPD^{850-1250}$ as a result of protein clustering. While the clusters formed were enriched in both VASP and $LPD^{850-1250}$ and predominantly uniform, we did notice some instances of in-homogeneity of protein fluorescence in the condensates (Fig. 2C), suggesting potential for layered organization within the condensates. Together these findings show that VASP and $LPD^{850-1250}$ are multivalent binding partners that undergo phase separation in a bulk solution and in a membrane milieu. As these proteins are important actin regulators[12,23,24,45,47], we decided to understand the role of phase separation in the polymerization of actin.

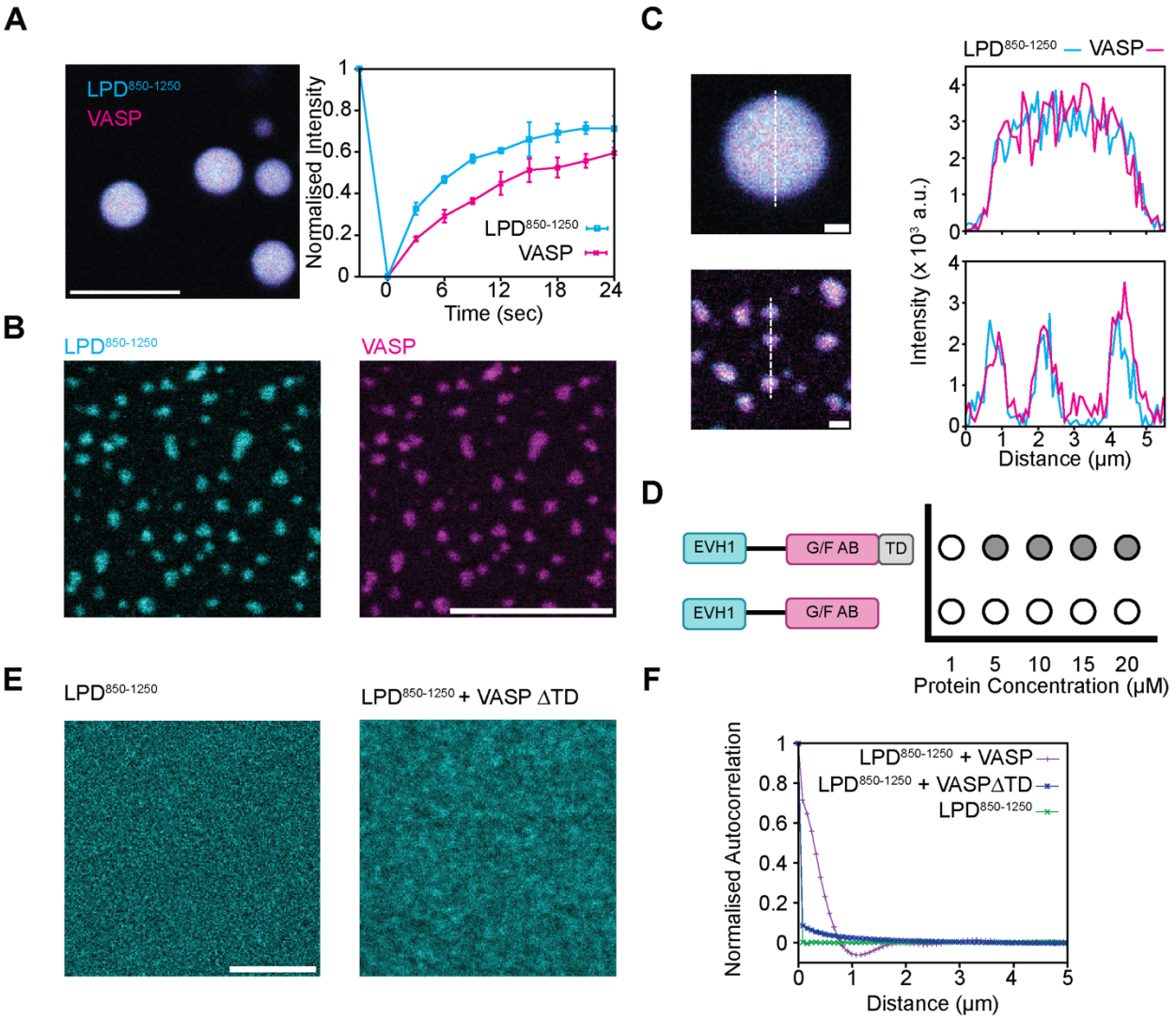

Figure 2: VASP forms liquid like condensates with membrane bound LPD$^{850-1250}$.

A) **Left** Liquid-like condensates formed by 20 µM VASP and 10 µM LPD$^{850-1250}$ doped with 1% Alexa-594 and Alexa-647 labelled VASP and LPD$^{850-1250}$ respectively. (scale bar 5 µm). **Right** Representative FRAP recovery curve for LPD$^{850-1250}$ and VASP in condensates corresponding to conditions described in **Left**. The error bars correspond to the standard deviation of 3 independent measurements.

B) SLB (1% Ni-NTA DOGS, 99% DOPC) coupled with 100 nM His tagged LPD$^{850-1250}$ after incubation with 2.5 µM VASP (doped with 250 nM Alexa 594 labelled VASP). Image acquired after 30 minutes of addition of VASP. Scale bar 5 µm.

C) Line intensity profile (**Right**) along dashed line (**Left**) drawn across LPD$^{850-1250}$ -VASP (10 µM LPD$^{850-1250}$ and 20 µM VASP with 10% labelled protein) droplet (top row) and clusters (100 nM LPD$^{850-1250}$ and 2.5 µM VASP) on a SLB (bottom row).

D) Phase separation behaviour of VASP (top row) and VASPΔTD (bottom row) with 10 µM LPD$^{850-1250}$. Filled and open circles represent cases where droplets were and were not observed, respectively. At least three independent experiments were performed.

E) Representative image of 100 nM His tagged LPD$^{850-1250}$ coupled to a SLB (1% Ni-NTA DOGS, 99% DOPC) before (**Left**) and after incubation with 2.5 µM VASPΔTD (**Right**). Scale bar 5 µm

F) Auto-correlation curves of LPD$^{850-1250}$, by itself, with VASP and VASPΔTD corresponding to concentrations mentioned in **B** and **E** respectively.

VASP- LPD$^{850-1250}$ condensates localize and enhance actin polymerization

The EVH2 domain of VASP is comprised of G and F-actin binding regions and a tetramerization motif that enables the protein to undergo liquid-like phase separation by itself[35] and allows for multivalent EVH1-FPPPP interactions that promotes LPD$^{850-1250}$-VASP demixing (Fig 2A, 2B). As biomolecular condensates provide improved spatiotemporal control of composition, regulation of protein activity and enzymatic reaction rates[29-31,51,52], we asked the question whether actin polymerization occurred predominantly within LPD$^{850-1250}$-VASP condensates (as opposed to their outside), and whether phase separated condensates accelerated the kinetics of F-actin formation.

We introduced actin, with a minority fraction labelled with rhodamine-green, to preformed LPD$^{850-1250}$ -VASP condensates and was allowed to polymerize at room temperature for 30 minutes. To minimize the extent of non-specific polymerization, a buffer lacking Mg^{2+} was used in the actin polymerization experiments[53]. Using confocal microscopy, we monitored the fluorescence intensity of labelled actin in the system over time. Within seconds of its introduction, we observed actin to strongly partition itself into the condensates (Fig 3A). As the system evolved, we noted a redistribution of the actin to the periphery of the condensate, forming a ring like actin structure driving a transition of the condensate from spherical topology to torus topology (Fig 3A-C). These transitions precede the formation of linear filaments (Fig 3E). To understand the relationship between the size of the condensate and the actin ring, we quantified the diameters of both the condensates (without actin) and the actin rings (after polymerization) observed in the system. When compared, we identified a shift in the size distribution of the actin rings to larger diameters with respect to LPD$^{850-1250}$ -VASP condensates (Fig 3D, Supplementary Fig. 4). We can appreciate this size increase by following the actin channel in Fig 3A where we can clearly see a flattening and concomitant widening of the condensate within 60s of the introduction of actin. Such ring-like actin structures have been previously observed in VASP condensates formed in the presence of the molecular crowding agent PEG[35]. Here we report the formation of actin rings in LPD$^{850-1250}$-VASP condensates formed in the absence of PEG, characterized by a peripheral distribution of not only actin but also of the condensate forming proteins (Fig 3B, 3C).

When stained with phalloidin (a small molecule that binds F-actin specifically), we observed specific binding of the phalloidin to the perimeter but not to the interior of the condensate (Fig 3F, 3G). This observation is consistent with the notion that F-actin while polymerizing in condensates, reorders itself along the perimeter to utilize the largest surface (the circumference) to grow along[35]. The extension of the filament by VASP and LPD$^{850-1250}$ within the condensate results in the bending of the F-actin due to actin's low persistence length (~15 μm). Eventually, we observed the emergence of linear actin filaments from the condensates (Fig 3E).

LPD and VASP have been seen to act synergistically to polymerize and bundle actin[12], however, it is unclear why this synergy exists. We wondered whether the tendency of proteins within phase separated condensates to exhibit increased activity [32] could explain LPD-VASP's synergy in polymerizing actin. We investigated this hypothesis using the

pyrene actin polymerization assay, which is based on the enhancement of pyrene fluorescence in filamentous actin compared to monomeric pyrene-labelled actin. Using protein mixtures of $LPD^{850-1250}$ with either the tetrameric VASP or the monomeric VASP-ΔTD, we isolated the contribution of multivalent $LPD^{850-1250}$-VASP interactions, a key driver of their phase separation, in their actin polymerization efficacy. Comparing the actin polymerization kinetics in the case of $LPD^{850-1250}$ with the VASP and VASP-ΔTD, we noticed a 4-fold decrease in pyrene fluorescence signal in the absence of multivalent interactions (Fig 3J). Therefore, the ability of $LPD^{850-1250}$ and VASP to interact multivalently and undergo LLPS is responsible for their increased ability to polymerize actin.

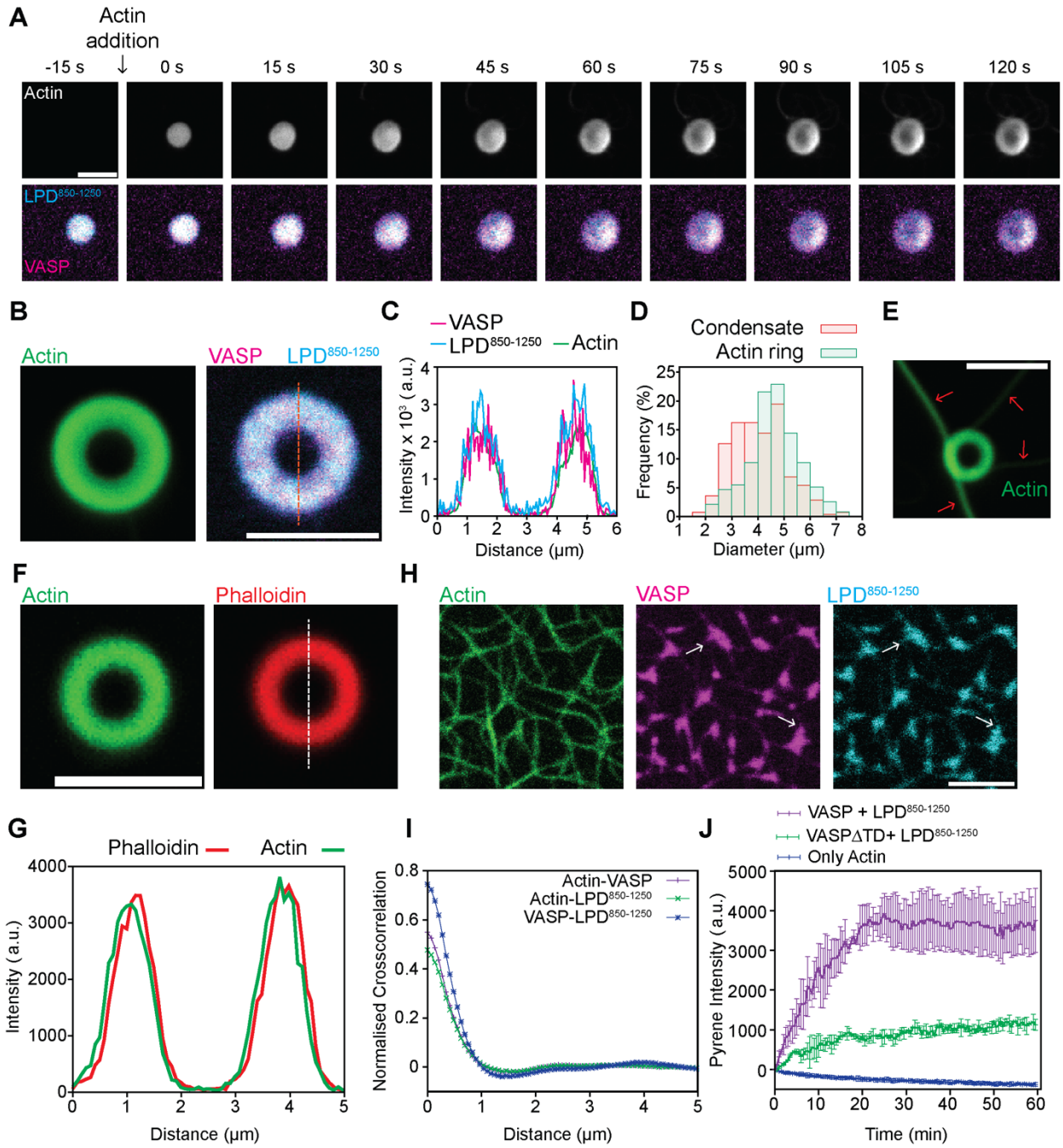

Figure 3: Condensates localize and enhance actin polymerization

A) Time evolution of actin (5 µM with 250 nM Rhodamine green actin) polymerized in condensates formed with 20 µM VASP and 10 µM LPD$^{850\text{-}1250}$ doped with 250 nM Alexa 594 and 647 respectively. Images acquired in intervals of 15 seconds show the time dependence of the peripheral distribution of actin and the concomitant deformation of the condensate. Scale bar 5 µm.

B) Actin (5 µm, doped with 250 nM Rhodamine green actin) polymerized within LPD$^{850\text{-}1250}$-VASP (10 µM, 20 µM respectively with 250 nM labelled protein each) condensates, imaged after 30 minutes of incubation. Scale bar 5 µm.

C) Line intensity profile along dashed line shown in **B**.

D) Size distribution of LPD$^{850\text{-}1250}$-VASP condensates and actin rings formed upon polymerization of actin within condensates. Condensates of composition 20 µM VASP (250 nM Alexa 594 labelled protein) and 10

μM LPD$^{850-1250}$ (250 nM Alexa 647 labelled protein) were incubated for 10 minutes after which actin (5 μM with 250 nM Rhodamine green labelled actin) or G-actin buffer of equal volume was introduced and incubated for 30 minutes. Diameter of condensates and rings were measured manually using ImageJ. $N_{condensates}$ = 277 and $N_{actin\ rings}$ = 236.
E) Instance of actin polymerization under conditions described in **A**, resulting in the formation of linear filaments from the condensates (Red arrows point to linear filaments). Scale bar 5 μm.
F, G) **F** Staining of F-actin in condensates prepared under conditions mentioned in **A** using Phalloidin Alexa 647. **G** Line intensity profile along dashed line shown in **F**. Scale bar 5 μm.
H) Actin (1 μM G-actin with 250 nM Rhodamine green G-Actin) polymerized on a SLB (1% Ni-NTA DOGS, 99% DOPC) with preformed His tagged LPD$^{850-1250}$ -VASP clusters (100 nM LPD$^{850-1250}$ and 2.5 μM VASP), showing deformation of clusters with pointed exit points for actin (White arrows point to a few examples in both the VASP and LPD$^{850-1250}$ channels). Imaged after 30 minutes of polymerization. Scale bar 5 μm.
I) Cross correlation plots of the pair-wise fluorescent channels (LPD$^{850-1250}$ -VASP, VASP-actin and actin-LPD$^{850-1250}$) corresponding to the image in **H**.
J) Kinetics of actin polymerization with LPD$^{850-1250}$ and VASP truncates was assessed using the pyrene fluorescence assay. LPD$^{850-1250}$, VASP and VASP-ΔTD were kept constant at 1 μM each and actin was used at 2 μM unlabelled doped with 250 nM pyrene labelled actin. The proteins were diluted in the G actin buffer (see methods), and actin was added immediately before the initiation of the experiment. The error bars represent the standard deviation of duplicates.

Actin polymerization deforms LPD$^{850-1250}$-VASP condensates

The polymerization of actin within the condensates resulted in the peripheral distribution of F-actin and the concomitant reorganization of the condensate to the edge (Fig 3B, 3C). The resulting torus was enriched in both actin and the proteins forming the condensate (Fig 3B, 3C). Similarly, actin polymerized from clusters of LPD$^{850-1250}$ and VASP on SLBs deformed the condensates (Fig 2B, 3H). As the F-actin exited the cluster, LPD$^{850-1250}$ and VASP moved along with the filament resulting in the formation of sharp edges (Fig 3H). We also observed an increase in the cross-correlation of LPD$^{850-1250}$ and VASP upon actin polymerization (Fig 2F, 3I), suggesting that actin polymerization increases LPD$^{850-1250}$-VASP co-clustering. These results suggest that irrespective of dimensionality, condensates undergo deformation as a result of actin polymerization possibly due to their preferred association with F-actin.

We decided to investigate the underlying nature of the interactions between the condensate and F-actin to identify the driving force for the protein reorganization along the filaments. As mentioned before, the filaments colocalized strongly with LPD$^{850-1250}$ and VASP, and we decided to test the mobility of the proteins on the actin filament by performing FRAP. We observed VASP and LPD$^{850-1250}$ to show recovery, albeit slower than in the absence of actin (Fig 2A, 4A, 4B), whereas the polymerized actin did not recover indicating the formation of a solid filament (Fig 4A, B). Together, these results demonstrate the presence of a mobile LPD$^{850-1250}$-VASP coat on the actin filaments and suggest that the condensates have wetted the actin filament.

Protein condensates interacting with substrates like the membrane,[54,55] or cytoskeletal structures like actin and microtubules[32] have been shown to undergo wetting transitions. To test whether the LPD$^{850-1250}$-VASP condensates were wetting the filament, we first polymerized actin in condensates like in Fig 3A, and subsequently incubated the system with latrunculin-A (LAT-A), a small-molecule actin depolymerase. We argued that, upon the depolymerization of F-actin within the condensates, a shape change should be

observed, with the condensates regaining their spherical shape as a result of the loss of its wetting surface. Consistent with this prediction, we observed the re-emergence of spherical droplets (Fig 4C, 5C) enriched in $LPD^{850-1250}$, VASP and actin. This result shows that the deformation of the condensates during actin polymerization is facilitated by wetting of F-actin by the condensates.

Finally, we were curious to understand why VASP and $LPD^{850-1250}$ showed slower mobility on actin filaments in comparison to the actin-free state (Fig 2A, 4B, 4E). To probe this, we performed FRAP on the LAT-A treated condensates. Interestingly, only actin and VASP showed an increase in mobility (Fig 4B, 4E) whereas $LPD^{850-1250}$ did not. This result is consistent with the prior observation that monomeric $LPD^{850-1250}$ does not interact with actin[12], and suggests that the VASP has a higher affinity for filamentous actin over monomeric actin.

Condensate dimensionality and surface interactions control F-actin morphology

A question that remained was why the F-actin structures obtained from the bulk condensates and membrane bound clusters have different morphologies. We had noted that actin polymerized in condensates resulted in ring-like actin structures (Fig 3B, 4F-ii) and those from the clusters on SLBs formed linear filaments (Fig 3H, 4F-i). We asked what factors influence the structural outcome. When comparing the bulk and the membrane systems, two key differences emerged. Condensates on the membrane tend to be significantly flattened (Fig Top row 4G-i, 4G-ii) relative to the spherically shaped droplets observed in the bulk before actin polymerization. We were curious to understand the contribution of the interaction of the condensates with a surface, and the dimensionality of the condensate prior to actin polymerization on the morphology of the filamentous actin obtained.

To decouple the role of the condensate's dimensionality and contact with a surface, we designed a series of complementary experiments. We polymerized actin in i) clusters formed on a membrane, ii) condensates in solution, iii) condensates tethered without wetting a coverslip, iv) condensates that were allowed to wet a coverslip (Fig 4G). The first and second cases have been described in previously (Fig 3B, 3H). We developed a new strategy to tether condensates to a surface. Briefly, the condensates were introduced to a Ni-NTA functionalised coverslip and were tethered to the surface via the His-tagged $LPD^{850-1250}$ present in the condensate (See Methods for details). This experimental setup allowed us to test the influence of contact with a surface when polymerization is initiated inside a spherical droplet (Fig 4G-iii). Upon the introduction of actin, we noticed rapid polymerization resulting in the formation of F-actin. However, unlike the bulk case (Fig 4F-ii), the tethered condensates formed a combination of ring-like and linear filaments (Fig 4F-iii), sharing features with the F-actin formed in the bulk (Fig 4F-ii) and on SLBs (Fig 4F-i). This result shows that the actin morphology can be altered by the contact of a condensate with a surface. We next tested the role of the dimensionality of the condensate in the fate of the F-actin morphology. To generate quasi-2D condensates from the bulk condensates, we let them wet a clean coverslip and subsequently introduced actin (Fig 4G-iv). Interestingly, actin polymerization from the wetted

condensates resulted in the exclusive formation of linear filaments (Fig 4F-iv). The ring structures obtained in the bulk and from un-wet condensates were not observed when the condensates were allowed to wet the glass. These results show that the condensates' dimension and contact with, and possibly interactions with, a surface are key factors that can alter the shape of the actin filament obtained from the vortex-like ring structure to linear actin filaments.

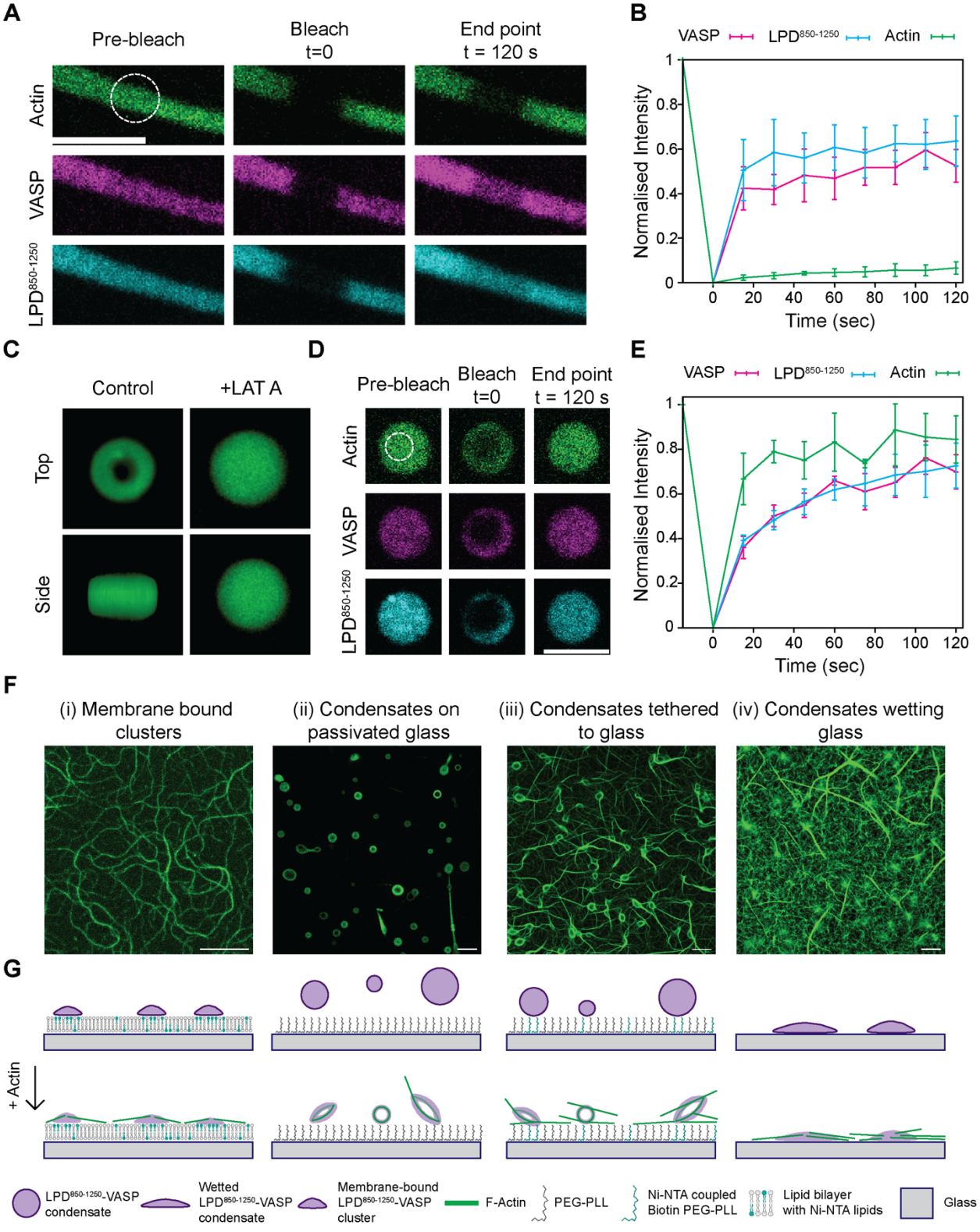

Figure 4: F-actin morphology is dictated by surface interactions and dimension of condensate.

A,B) A Images depicting the recovery upon photobleaching of actin filaments (Bleach area within the white dashed circle) formed from condensates and $LPD^{850-1250}$-VASP proteins (20 μM VASP, 10 μM $LPD^{850-1250}$ and 5 μM Actin). **B** Plot depicting the corresponding normalised fluorescence recovery profiles. Scale bar 5 μm.
C) Top and side views of a 3D reconstruction created from a Z-stack of actin polymerized in $LPD^{850-1250}$ -VASP condensates before (**Left**) and after treatment with Latrunculin A (**Right**).
D,E) D Image series and **E** normalised fluorescence recovery curves of $LPD^{850-1250}$-VASP condensate and actin (20 μM VASP, 10 μM $LPD^{850-1250}$ and 5 μM Actin) treated with LAT-A (5μM). Experiment performed 30 minutes after the introduction of LAT-A. The bleached area is enclosed by the dashed white circle. Scale bar 5 μm.
F) Actin polymerized from condensates **i**) on SLBs, **ii**) condensates in the solution, **iii**) condensates tethered to a glass surface, and **iv**) condensates allowed to wet a glass surface. 100 nM $LPD^{850-1250}$, 2.5 μM VASP and 1 μM Actin (10% rhodamine labelled actin) used for **i**, 20 μM VASP, 10 μM $LPD^{850-1250}$ and 5 μM Actin (100 nM rhodamine labelled actin) used for **ii-iv**. Scale bar 10 μm.
G) Schematic depicting actin morphologies obtained from polymerizing actin from $LPD^{850-1250}$ -VASP condensates described in **F**. Legend included at the bottom of the schematic.

EDP suppresses VASP mediated actin polymerization

VASP enables the polymerization of actin during the formation of filapodial projections when recruited to the plasma membrane by the inverse-BAR (I-BAR) domain containing protein IRSp53[42,56]. Interestingly, it has been observed that VASP's actin polymerization efficacy is decreased by its binding to IRSp53[42]. We wondered whether, in the context of FEME, EDP, an N-BAR protein, had similar antagonistic effects on VASP mediated actin polymerization. To probe the role of EDP, we tested the polymerization of actin in condensates composed of EDP, $LPD^{850-1250}$ and VASP. In comparison to the case lacking EDP, where actin rings and toroid condensates were formed (Fig 3B), here we observed uniform actin intensity in condensates that retained a spherical shape (Fig 5A, 5C). To investigate the structure of actin within the condensates, we decided to simultaneously visualize both monomeric and filamentous actin by using rhodamine-green labelled actin and an orthogonally labelled Alexa Fluor™647-Phalloidin, an F-actin specific stain. Consistent with the uniform actin fluorescence, we observed minimal staining of phalloidin inside the condensates with a few thin actin filaments distributed peripherally (Fig 5B). This observation suggests that actin polymerization is suppressed, but not abolished by the presence of EDP in the condensates.

Actin (doped with Pyrene labelled actin) was polymerized in the presence of $LPD^{850-1250}$-VASP, with and without EDP, and the pyrene fluorescence was monitored to assess the contribution of EDP on the polymerization kinetics and amount of polymerized F-actin. From the growth curves, it is evident that in the presence of EDP, the maximum pyrene fluorescence was 5-fold lower, corresponding to lower actin polymerization, than compared to the absence of EDP (Fig 5E). Together, these results show that EDP, a key initiating protein in FEME, strongly antagonizes $LPD^{850-1250}$-VASP mediated actin polymerization.

Multivalent EDP-VASP interactions negatively regulate actin polymerization

As EDP's presence in $LPD^{850-1250}$-VASP condensates resulted in a suppression of actin polymerization, we were interested in understanding the mechanism of EDP's new function. To this end, we designed various EDP related model proteins to investigate domain specific contributions and the role of multivalency in the suppression of actin polymerization. As EDP undergoes homotypic LLPS mediated by its NBAR domain, to mimic the increased valency of EDP, we designed a pentameric SH3 construct, here on referred to as $(SH3)_5$, with the individual SH3 domains concatenated by the native EDP linker. The individual N-BAR and the SH3 domains of EDP, and $(SH3)_5$ were used in the following experiments. We introduced these EDP constructs into $LPD^{850-1250}$-VASP condensates at identical concentrations to that of full length-EDP (Fig. 5A) and studied the capacity of the condensates to polymerize actin. From Figures 5A, 5D, we can see that both the SH3 and N-BAR domains by themselves were unable to confer the reduction of actin polymerization observed with the full-length protein (5A, 5D). Interestingly, only the pentameric $(SH3)_5$ was able to recapitulate the antagonizing influence of EDP (5A, 5D).

To confirm the contribution of multivalent interactions with EDP on VASP's capacity to polymerize actin, we performed a pyrene assay with VASP and $(SH3)_5$. We observed that in the presence of $(SH3)_5$, VASP was unable to polymerize actin (Fig 5F). From the above, we can conclude that the multivalent interactions between EDP's SH3 domain and VASP's EVH1 and EVH2 domains result in the loss of VASP's actin polymerization potency.

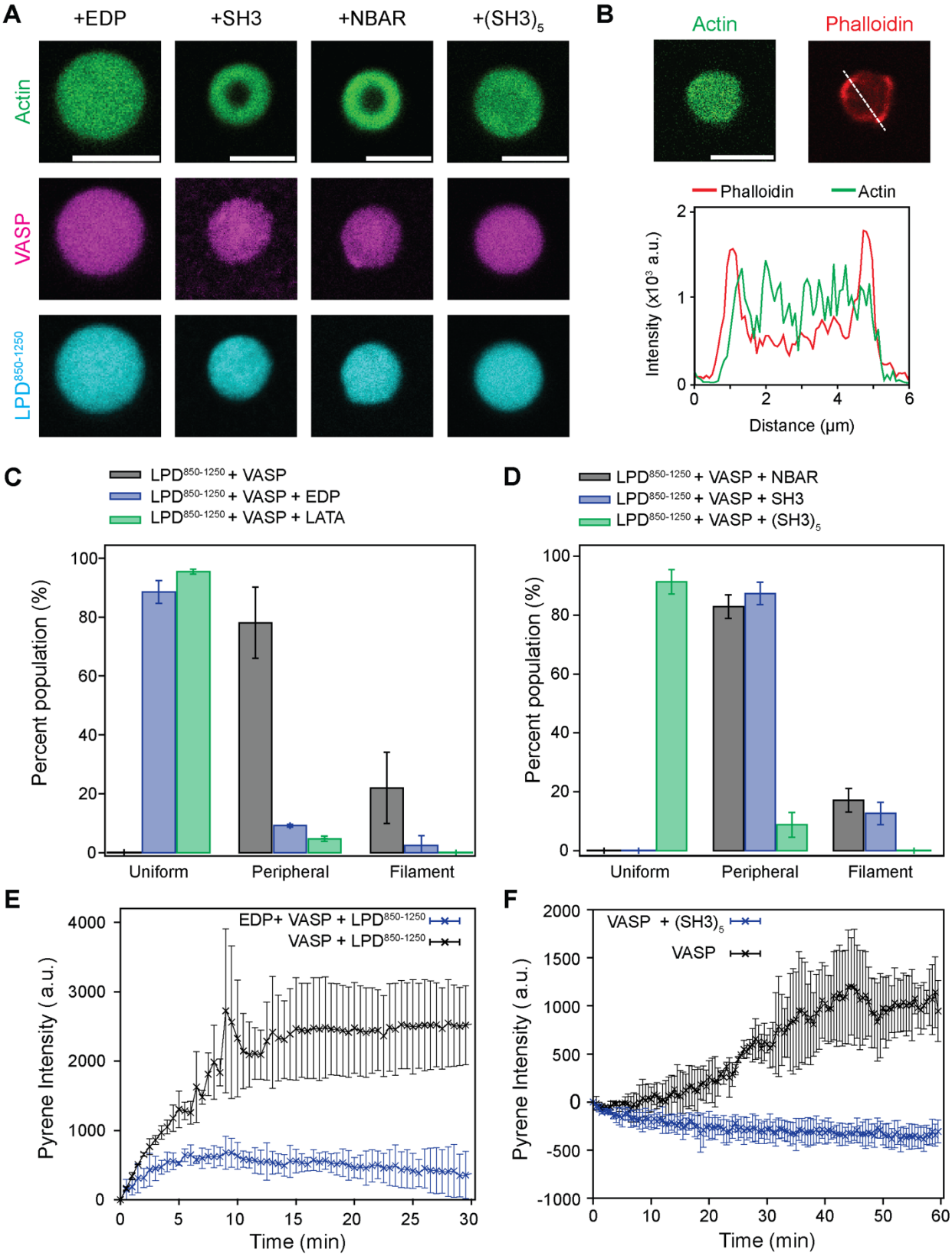

Figure 5: EDP suppresses VASP mediated actin polymerization

A) Actin (5 μM) polymerized in condensates made of EDP constructs (full-length EDP, monomeric SH3 and NBAR domains, and $(SH3)_5$), VASP and $LPD^{850-1250}$ (concentrations used were 40 μM EDP/SH3/NBAR, 20 μM VASP with 250 nM Alexa-594 labelled protein,10 μM $LPD^{850-1250}$ with 250 nM Alexa-647 labelled protein). In the case of $(SH3)_5$, 8 μM protein was used as it corresponds to 40 μM of monomeric SH3. Experiments with EDP and $(SH3)_5$ showed uniform actin fluorescence intensity, suggesting lack of actin polymerization. Images acquired after 30 minutes of polymerization. Scale Bar 5 μm.
B) **Top** Staining filamentous actin polymerized in $LPD^{850-1250}$-VASP- EDP condensates (corresponding to conditions mentioned in **A** using phalloidin. The proteins in the condensate were kept unlabelled. Actin was doped with 250 nM Rhodamine green actin and Alexa-647 labelled Phalloidin were used. Images acquired after 30 minutes of phalloidin treatment. **Bottom** Line intensity profile along white dashed line shown in the phalloidin channel (**Top**). Scale Bar 5 μm.
C) Percentages of actin morphologies observed after polymerization in condensates. Actin was polymerized in 10 μM $LPD^{850-1250}$ and 20 μM VASP condensates (grey bar, N =88), with 40 μM EDP (blue bar, N=76) or 5 μM LAT-A (green bar, N = 66). Categorization was performed based on inspection of the actin distribution in the condensates. Isotropic actin intensity was categorised as **Uniform**, ring-like distribution as **Peripheral**, and linear structures as **Filament**. Images were acquired after 30 minutes of polymerization.
D) Quantification of the abundance of actin structures (uniform, peripheral or filament) in conditions corresponding to **A (columns 2-4)**. Number of condensates analysed for the individual cases were $LPD^{850-1250}$ and VASP with SH3 monomer (blue bar, N=53), with NBAR (grey bar, N=70) and with $(SH3)_5$ (green bar, N=143).
E, F) Actin polymerization kinetics (2 μM G actin + 250 nM Pyrene actin) in the presence of **E)** 1 μM $LPD^{850-1250}$, 1 μM VASP +/- 5 μM EDP and **F)** 1 μM VASP +/- 1 μM EDP $(SH3)_5$. Error bars correspond to standard deviation of 3 independent measurements.

Interaction of EDP and $LPD^{850-1250}$ with plasma membrane biomimetic bilayers facilitates the recruitment and clustering of VASP

VASP's recruitment to the leading edge has been suggested to occur via membrane bound adaptor proteins, including IRSp53[42] and LPD[23] whose recruitments are phosphatidylinositol (PIP) lipid dependent[23,57]. Amongst negatively charged lipids in the plasma membrane, PIP lipids contribute to a minority fraction while phosphatidylserine (PS) lipids are the most abundant[58]. As $LPD^{850-1250}$ is very positively charged (net +17 charge), we wondered if it could interact with bilayers containing PS lipids. We investigated the recruitment of $LPD^{850-1250}$ to giant unilamellar vesicles (GUVs) comprised of 25/30/45 mol percent zwitterionic 1,2-Dioleoyl-sn-glycero-3-phosphocholine (DOPC) and 1,2-dioleoyl-sn-glycero-3-phosphoethanolamine (DOPE), and anionic 1,2-dioleoyl-sn-glycero-3-phospho-L-serine (DOPS) lipids, a model membrane composition used to mimic the inner leaflet of the plasma membrane. We observed uniform binding of $LPD^{850-1250}$, when co-incubated with the anionic GUVs (Supplementary Fig. 5), suggesting the tail of LPD could act complementarily with its PH domain to engage with the plasma membrane.

Since EDP is also known to interact with vesicles comprised of the above described lipid composition[59], we wondered if either EDP or $LPD^{850-1250}$ could recruit VASP to plasma membrane mimicking bilayers. Interestingly, the vesicles incubated with VASP in the presence of either $LPD^{850-1250}$ or EDP showed strong recruitment of VASP (Figure 6A, 6B, 6C). Similar to the interaction of $LPD^{850-1250}$ and VASP on the SLBs (Figure 2B), we observed non-homogeneous clustering of both VASP- $LPD^{850-1250}$ and VASP-EDP on the

GUVs (Figure 6D). Interestingly, the recruitment of VASP by EDP also resulted in the formation domains on GUVs (Figure 6B, 6D). The ability of VASP to cluster has been observed in microspike[45] and filopodial protrusions[47,56], and this clustering is thought to enhance VASP's actin processivity. We therefore were interested in investigating the ability of VASP clusters formed with EDP and LPD$^{850-1250}$ to polymerize actin on plasma membrane mimicking GUVs.

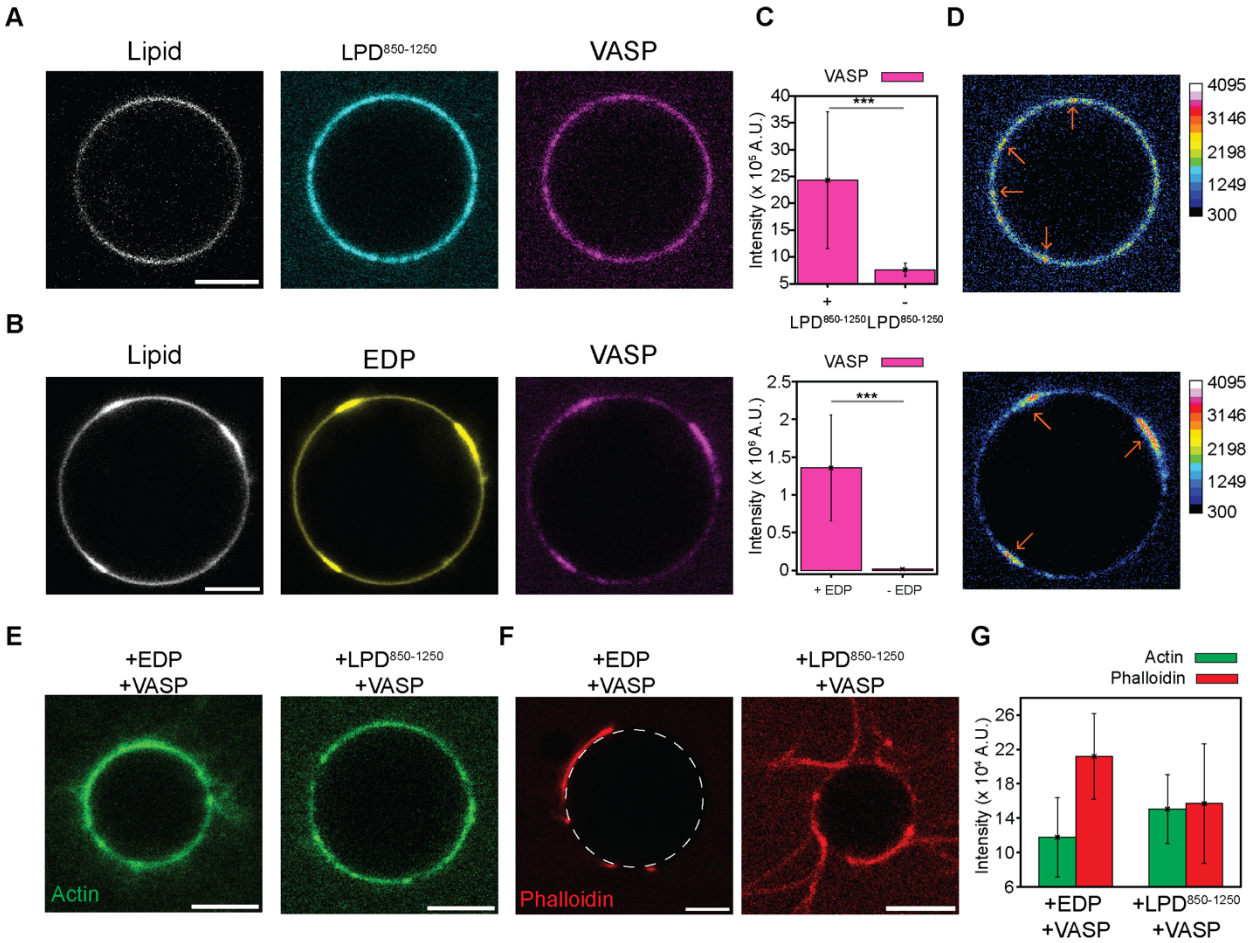

Figure 6: Recruitment of VASP to anionic lipid bilayers by LPD$^{850-1250}$ or EDP enables membrane proximal actin polymerization.

A,B) Recruitment of VASP (1μM VASP with 10% Alexa 594 labelled VASP) to GUVs of lipid composition that mimic the inner-leaflet of the plasma membrane (45:30:24:1 mol% DOPS:DOPE:DOPC:MB-DHPE) in the presence of A) LPD$^{850-1250}$ (1 μM LPD$^{850-1250}$ with 10% Alexa 647 labelled LPD$^{850-1250}$) and B) EDP (2μM EDP with 5% Alexa 488 labelled EDP). Scale bar 5 μm.

C) Intensity of VASP in clusters on GUVs corresponding to conditions described in A, B respectively. Error bar corresponds to +/- 1 standard deviation. Analysis: unpaired student t test was performed with a P value of < 0.005 (***).

D) Intensity based colouring of images shown in **A, B** depicting clustering of VASP on GUVs when recruited by LPD$^{850-1250}$ (Top) and EDP (Bottom). Orange arrows point to regions of clustering on GUVs.

E) Representative images of actin polymerized (5μM G-actin with 250 nM Rhodamine green labelled G-actin) on GUVs in the presence of (2μM) EDP and **Left**, VASP (1μM) or **Right**, LPD$^{850-1250}$ (1μM) and VASP (1μM). Scale bar 5 μm.

F) Representative images of GUVs corresponding to conditions described in E, stained with Alexa 647 labelled phalloidin. The white dashed circle represents the location of the GUV. Scale bar 5 µm.
G) Fluorescence intensity of actin and phalloidin on GUVs corresponding to cases described in **F**.

Membrane associated VASP-clusters recruit and polymerize actin

The recruitment and polymerization of actin at FEME priming sites is essential for the completion of endocytosis. Utilizing the biomimetic GUV system described in the previous section, we assessed the ability of VASP to polymerize actin in an inner leaflet-like environment. VASP was recruited to the membrane either using $LPD^{850-1250}$ or EDP as the adaptor protein, and actin polymerization on the membrane was initiated. We observed the recruitment of actin to the GUVs in both cases (Fig 6E) and interestingly even observed filaments emanating away from the surface of the vesicles (Fig 6E). We stained the actin covered GUVs with fluorescently labelled phalloidin, and consistent with the presence of F-actin, we observed strong phalloidin signal on the vesicles (Fig 6F, G). It is worth mentioning that EDP mediated recruitment of VASP did not appear to negatively influence actin polymerization on the vesicles, unlike the bulk system where EDP suppressed VASP's activity (Fig 5A, 6E). We suspect this difference in EDP's influence on VASP mediated actin polymerization is dictated by EDP's interaction with negatively charged bilayers. EDP is known to bind and generate tubules from anionic lipid membranes (including the composition used here) and sort itself to these regions of high curvature[60-62]. We suspect that, in our experiments, the charged lipid membrane with local curvature sequesters EDP, relieving its inhibitory effect on VASP, allowing actin polymerization to occur.

Discussion

The actin machinery involved in the clathrin-independent pathway of FEME has thus far been understudied. In this contribution, we show that VASP, a member of the Ena/VASP actin polymerases, is a novel EDP binding partner that co-localises at FEME priming patches at the cellular leading edge. We further show that the key FEME proteins LPD and EDP interact multivalently with VASP to form liquid-like condensates. LPD and VASP condensates act as reaction centres that localise and promote actin polymerization. We find that the dimensionality and consequently the shape of the condensate plays a critical role in the morphology of the F-actin obtained. We demonstrate that multivalent interactions between EDP and VASP act as a negative regulator of VASP mediated actin polymerization that is relieved by EDP's interaction with deformable anionic lipid membranes, providing a novel function for EDP. Finally, we show that in the presence of a lipid bilayer mimicking the inner leaflet of the plasma membrane, LPD and EDP can recruit and cluster VASP allowing for spatially localised, membrane-proximal actin polymerization.

As biological systems exist in a non-equilibrium state with numerous dynamic processes occurring simultaneously[63], the preservation of spatial symmetry is inconceivable. The loss of uniformity with concomitant formation of more structured states is a result of a process known as symmetry breaking. In biology, symmetry breaking is essential and can

be observed from the scale of molecular assemblies to the organization of the actin cortex[64,65], to macro scale structure and development[66]. One result of such symmetry breaking in-cellulo is in the formation of actin filaments, asters, and ring structures, that are commonly seen on the plasma membrane in different physiological contexts. Asters are seen in the actin cortex[67], the network of actin filaments bound to the plasma membrane. Ring morphologies have been observed in micron sized contractile rings[68] and nano-scale structures at the base of endocytic buds[69-71].

Interestingly, simulations and experiments have shown that the spatial confinement of actin facilitates symmetry breaking, allowing for the formation of organised structures[72,73]. In our system, actin polymerization is initiated within the confined volumes of quasi-2D and 3D condensates, suggesting a possible role for symmetry breaking. Taking a closer look at the individual stages of actin polymerization, we see that upon the initiation of polymerization, short filaments are formed within the condensates (Fig 7A-i), allowing for isotropic distribution of the F-actin. This uniformity is lost upon the progression of actin polymerization resulting in the partitioning of longer filaments to the periphery of the condensate (Fig 7A-ii). As shown in Fig 8, and consistent with previous observations[35], we believe that actin filaments align tangentially within the condensate torus, as opposed to radial alignment[70]. Continued elongation of F-actin results in the formation of a shell-like structure resembling a cortical actin network (Fig 7A-iii). A likely reason for the peripheral distribution of actin within the condensate is that F-actin bends at the periphery of the condensate due to its low persistence length of around 5-20 μm[74].

With continued polymerization and bundling, the actin shell state rapidly collapses to form an actin ring along an arbitrary axis (Fig 7A-iv) resulting in a change from 3D to 2D radial symmetry. Concomitantly, the condensate flattens initially forming a disk that transitions into a torus shape, containing, and thus completely wetting, the actin ring (Fig 7A-v). It can be shown that, above a critical radius, a torus has a smaller surface area relative to a disk with the same volume. We therefore believe that condensates above that critical radius undergo a disk-to-torus transition in order to minimize interfacial energy. Our findings suggest that contact of the condensate with a surface might bias the orientation of the ring such that the ring makes contact with the underlying interface (Fig 4G-iii). Continued polymerization and bundling of F-actin triggers the emergence of linear filaments from the ring, causing a loss of radial symmetry (Fig 7A-vi). Our results differ in two important ways from recent observations of actin polymerized in VASP droplets induced by PEG-mediated crowding[35,75]. In their findings, the formation of actin shells was observed to be predominant, and a morphological transition to torus-like shapes was not observed. According to Chandrasekaran et al., actin rings are formed preferentially instead of shells in the presence of strong F-actin cross-linking[75]. This cross-linking enhancement in our system is likely achieved by LPD's capacity to bundle actin with VASP[12], directing the actin organization towards ring morphologies over shells. Building on recent observations[35], our findings experimentally demonstrate that the confined polymerization of actin within LPD$^{850\text{-}1250}$-VASP condensates occurs through a series of spontaneous symmetry breaking events.

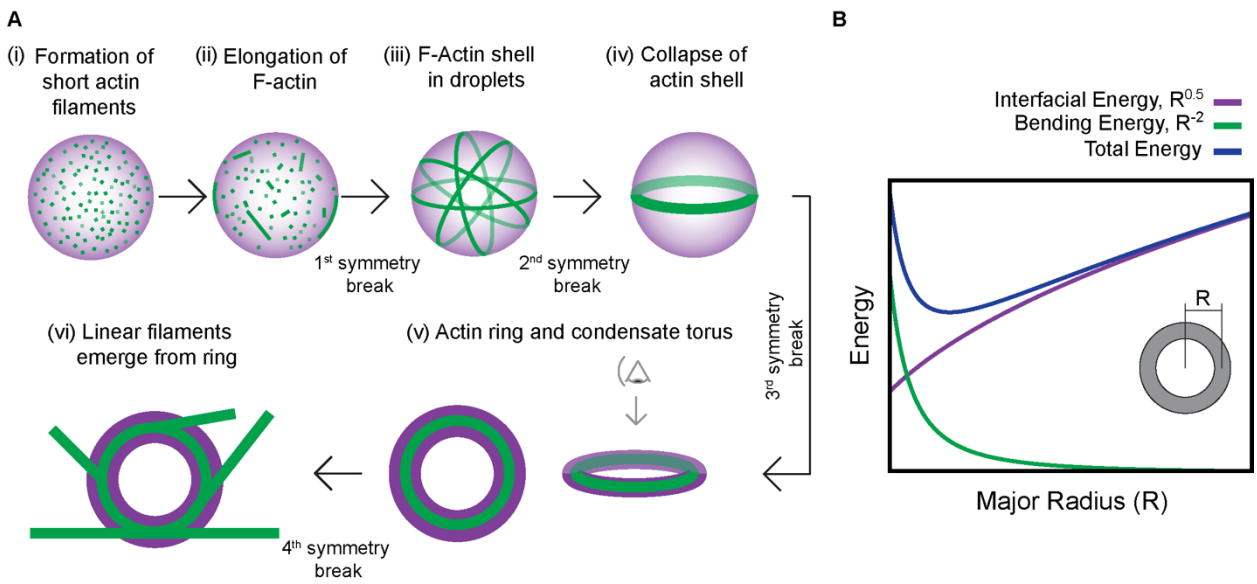

Figure 7: Actin polymerization within condensates: morphological changes and energetic considerations.

A) Schematic of confined actin polymerization and concomitant morphological changes in $LPD^{850\text{-}1250}$-VASP condensates in the bulk:

i) Actin polymerization within $LPD^{850\text{-}1250}$-VASP condensates (purple spheres) generates short filaments (green squares). F-Actin distribution is isotropic at this stage.

ii) Progression of polymerization of F-actin (green rods) creates inhomogeneity of actin distribution. Short filaments remain in the interior of the condensate whereas longer filaments align themselves along the perimeter of the condensate.

iii) Elongated filaments decorate condensate along the periphery forming a short-lived shell-like structure.

iv, v) Collapse of the actin shell to a single axis, forming a ring (iv) and concomitant reshaping of the protein condensate to adopt a torus structure (v).

vi) Formation of linear filaments and bundles of F-actin from rings along the plane of the ring.

B) Plot representing the form of the interfacial energy of a torus of fixed volume with a variable major radius R ($\propto R^{0.5}$, Purple curve), the bending energy of an actin filament of fixed length confined within a torus of variable major radius ($\propto R^{-2}$, Green curve), and the sum of the two contributing energy terms ($\propto R^{0.5} + R^{-2}$, Blue curve) depicting a minima suggesting a preferred radius of the torus. The major radius is defined as the distance between the centre of the structure and the mid-point of the rim. The cartoon drawn on the top left pictorially indicates the definition of the torus' major radius.

The energetic cost of accommodating an actin filament (of length L) within a condensate torus is the sum of the actin filament bending energy and the condensate interfacial energy, expressed as

$$E = \frac{1}{2} L K \frac{1}{R^2} + \sigma A \qquad 1$$

Where E is the total energy, K is the bending stiffness of the actin filament, σ is the surface tension of the condensate, R is the radius of curvature of the filament (assumed to be equal to the major radius of the torus, Fig 7B), and A is the surface area of the torus.

Using expressions for the surface area ($A = 2\pi r \times 2\pi R$) and volume of a torus ($V = \pi r^2 \times 2\pi R$), where R and r are the major and minor radius of the torus respectively, we can rewrite Eq. 1, assuming constant volume, as a function of only the major radius of the torus,

$$E(R) = \left(\frac{LK}{2R^2}\right) + 2\pi\sqrt{2VR} \qquad 2$$

To illustrate the influence of the torus radius on the interfacial and bending energies, we plot a simplified form of Eq. 2 assuming the coefficients of the R^{-2} and $R^{0.5}$ terms to be equal to 1 (Fig 7B, purple and green curves). The sum of the two contributions, which can be used as a proxy for the total energy (Fig 7B, blue curve), shows an energy minimum suggesting the presence of a preferred size of torus. Minimization of Eq. 2 with respect to R yields,

$$R_{min} = \left(\frac{LK}{\pi\sigma\sqrt{2V}}\right)^{\frac{2}{5}} \qquad 3$$

While Eq. 3 provides a relationship between the volume of the condensate (V) and the resultant torus radius upon actin polymerization (R_{min}), incorporation of additional considerations may be needed to obtain a more accurate estimation of R_{min}. These include the amount of actin and ATP available in the system[35], accounting for the presence of multiple filaments and bundles in a condensate and the influence of bundling on the bending stiffness of actin. As our experiments' resolution is constrained by the diffraction limit, super-resolution microscopy techniques can be employed to obtain information on smaller actin architectures formed in-vitro and in-cellulo. Based on our experiments (Fig. 3D, Supplementary Fig. 6) and calculations, we believe that condensate size may be one of the important parameters that can modulate the morphology of the actin architecture formed around endocytic buds.

The capacity of EDP-A1, LPD$^{850\text{-}1250}$ and VASP droplets to polymerize actin, an energy consuming step, generating stresses within the condensate showcase the hallmarks of an active material. In FEME, the priming patches consist of EDP-A1-2 enriched short-lived clusters on the plasma membrane. In the absence of receptor activation, they dissolve and reform elsewhere on the plasma membrane, thereby scanning the surface for cargo to internalise[41]. Similarly, LPD-VASP clusters formed at the leading edge are dynamically unstable as they undergo fission in a size dependent manner, and are stabilised by their interaction with F-actin[47]. Our finding that EDP-A1, LPD$^{850\text{-}1250}$ and VASP containing condensates mimicking FEME priming patches can locally polymerize actin, with the extent of actin polymerization being controlled by the condensate composition, resulting in the deformation, and reshaping of protein condensates (Fig 6, Fig 7A, Fig 8), suggests that FEME priming patches might be active droplets. Actin-containing droplets formed in the presence of cross-linkers like filamin and motors such as Myosin[76], and with its regulators during the maturation of oocytes[77] have been previously shown to behave like active condensates. Collectively, we propose that the VASP rich FEME priming patches are active droplets that exhibit dynamic instability

allowing for their rapid formation and dissolution without undergoing coarsening and are stabilised by the local actin polymerization undergoing active remodelling (See Fig 8). Such a mechanism could work in conjunction with other mechanisms of priming patch dissolution including regulation by Cdc42-GAPs[19].

Finally, we propose a model describing how actin polymerization in membrane-associated condensates may couple with membrane curvature generation in FEME. Our findings show that priming patch mimics consisting of LPD-VASP-EDP condensates locally initiate actin polymerization. However, the formation of long filaments is suppressed due to EDP's role antagonistic to actin polymerization. At this stage the condensates may be dynamically unstable[77] with spontaneous formation and dissolution of priming patches (Fig 8 A, B). Alternatively, the transient nature of FEME priming patches might be described by spontaneous composition fluctuations near a critical mixing point[78,79]. Collectively, this dynamic nature of priming patches is indicated by the double arrow (T1) in Fig 8.

Upon the triggering of FEME through activation of receptors that interact with EDP, such as the β1A-receptor[80], we anticipate the sorting of EDP to the emerging bud (Fig 8C). This sorting is facilitated by the recognition of high membrane curvature by EDP and by its binding to the activated receptor. A consequence of this is the depletion of EDP from the LPD-VASP condensate, initiating the rapid polymerization of actin around the bud. We suspect that VASP's enhanced polymerization efficacy when clustered[12,81] could also play a supportive role in the formation of actin rings at the base of the bud. The topological transition of the condensate from spherical to torus topology is indicated by the single arrow (T2) in Fig 8. Interestingly, the size of the endocytic carriers formed in FEME (~ 1 μm)[3] and the condensate/actin torus formed in our experiments (~ 4-5 μm, Fig 3A and 3D) are within an order of magnitude of each other. The remaining discrepancy can be explained based on the relationship between the size of the condensates and the ring formed upon the polymerization of actin. From our experimental results and simple model (Eq. 3), we believe that the volume of the condensate dictates the size of the torus formed upon actin polymerization (Fig 3D). Therefore, in FEME, we expect the formation of smaller actin rings upon the initiation of endocytosis due to the smaller size of the priming patch. Subsequent branching induced by N-WASP and Arp2/3 may then allow for the radial growth of actin around the base of the bud to facilitate elongation and fission. Supported by theoretical[82,83] and experimental evidence[71], we believe that the ring-like polymerized actin, can provide a mechanical force by pushing against the plasma membrane and by interacting with the bud and the surrounding actin network, facilitating budding and fission.

Collectively, informed by our findings, the proposed model describes a possible mechanism of spatiotemporally controlled actin polymerization coupled to the initiation of endocytosis in FEME.

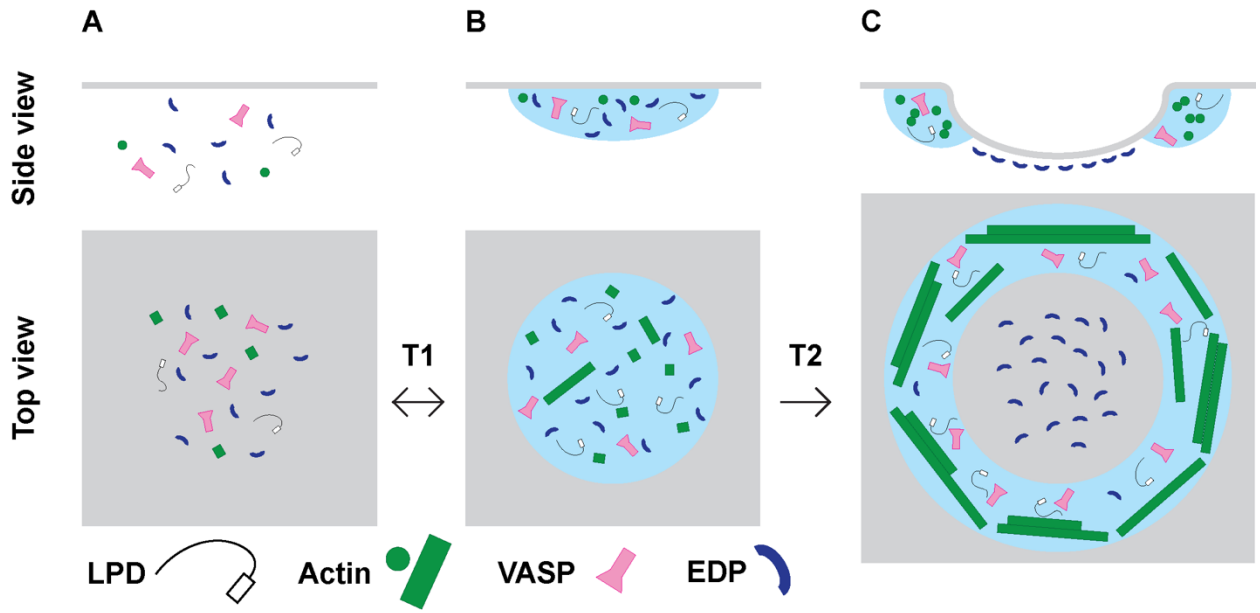

Figure 8: Proposed model for the initiation of actin polymerization on the plasma membrane in FEME.
T1: Transition between formation (**B**) and dissolution (**A**) of FEME priming patches dictated by dynamic instability of condensates.
T2: Transition depicting depletion of EDP from condensates and enrichment at the emerging bud mediated by receptor activation (receptor not shown). Concomitant downhill transition with actin polymerization at the base of bud in LPD-VASP rich condensate forming ring structures. Final state shown in **C**.

Materials and Methods

Reagents

Fluorophores used were Alexa Fluor™−488 C5-maleimide, Alexa Fluor™−488 5-SDP ester, Alexa Fluor™ 594 succinimidyl ester and Alexa Fluor™647 succinimidyl ester and were purchased from Invitrogen. Latrunculin A (Cayman) Alexa Fluor™ 647 Phalloidin (Invitrogen) were used in the actin depolymerization and staining respectively. Pyrene actin was purchased from Cytoskeleton.
Lipids used namely, 1,2-dioleoyl-sn-glycero-3-phosphocholine (DOPC), 1,2-dioleoyl-sn-glycero-3-phosphoethanolamine (DOPE), 1,2-dioleoyl-sn-glycero-3-phospho-L-serine (DOPS) and 1,2-dioleoyl-sn-glycero-3-[(N-(5-amino-1-carboxypentyl) iminodiacetic acid) succinyl] (nickel salt) (Ni-NTA DOGS) were acquired from Avanti Polar lipids (USA). Fluorescent lipids used in the study were Marina Blue™ 1,2-Dihexadecanoyl-sn-Glycero-3-Phosphoethanolamine (Marina Blue™ DHPE) (Invitrogen) and Forte Blue DHPE (AAT Bioquest).
HEPES, NaCl, Na_2HPO4, NaH_2PO_4, DTT, IPTG, glutathione, EDTA were purchased from Fisher Scientific. Glycerol and ATP-Mg, Polyethlene glycol (avg. MW 8000) were purchased from Sigma Aldrich, Imidazole from Acros organics and Pierce™ TCEP-HCl from Thermo Scientific. Passivating agents used were Bovine serum albumin (BSA) (Fatty acid free, fraction V) (MP Biomedicals) and β-Casein (Thermo Fisher Scientific).

PEG-PLL was a kind gift from Elizabeth Rhoades. Restriction enzymes and T7 ligase were purchased from New England Biolabs.

Plasmids

Bacterial expression plasmids

Sequences coding for $LPD^{850-1250}$, VASP, and Rat EDP A2 were synthesized (Biomatik) and inserted into PGEX-6P1 vectors, whereas the EDP A1 linker (SH3)5 was cloned into a PMAL vector with an N and C terminal TEV cleavage site for the MBP and 6xHis tags respectively. VASP ΔTD (AA 1-335), and EVH1 (AA 1-113) were cloned using the VASP plasmid as the template. DNA encoding for Rat EDP A1 (single cysteine mutant) (EDP-A1), SH3, NBAR, ΔSH3 were inserted into the PGEX-6P1 vector, and its generation is described elsewhere[84].

Mammalian expression plasmids.

VASP (pEGFP-C1-VASP) was a kind gift from Tatyana Svitkina. VASP and its truncates EVH1 (AA 1-113), linker (AA 114-224) and EVH2 (225-380) were cloned into the mScarlet vector.

Confocal Microscopy

An Olympus IX83 inverted microscope equipped with a 60x 1.2 NA water immersion objective (Olympus) and a FluoView 3000 scanning system (Olympus, Center Valley, PA) was employed for confocal microscopy and FRAP studies. Sequential line scanning was implemented when imaging samples with multiple fluorophores (Marina blue, Alexa 488, Alexa 594, and Alexa 647) to cross-talk between channels. Images were analysed using Fiji and python (v 3.7.1).

For condensate and actin polymerization studies, coverslips (25 mm, Fisher Scientific) were cleaned by bath sonication in 2% Hellmanex, followed by three washes with water. The cleaned coverslips were either used immediately or stored in 200 proof ethanol until they were needed. The coverslips were passivated by creating a PEG-PLL coating following the protocol described elsewhere[85]. The sample to be imaged was deposited in the centre of the coverslip and a closed imaging chamber was created by sandwiching another coverslip on top with a thin layer of vacuum grease (Molykote, Dupont) around the edge.

BSC1 cell culture:
BSC1 cells were cultured at 37°C 10% CO2 in DMEM (Sigma) supplemented with 10% FCS and Penicillin / Streptomycin. Cells were plated on uncoated glass coverslips for immunofluorescence experiments at a density of approximately 2.5×10^4 cells per coverslip.

HeLa culture and lysate preparation

HeLa cells were cultured in DMEM supplemented with 10% fetal bovine serum (FBS), and 1x Penicillin-Streptomycin antibiotic. For generating cell lysate, the cells were seeded on 100 mm dishes and transfected with 2-3 µg of DNA at 80% confluency. Cells were harvested in cold DPBS after 24 h of over-expression and lysed by tip sonication.

Immunofluorescence

Cells were left to spread on glass coverslips for 6 hours and were fixed with 4% PFA in PHEM buffer (60mM PIPES, 25mM HEPES, 10mM EGTA, 2mM $MgCl_2.6H_2O$, 0.12M sucrose) for 20 minutes at 37°C. Fixed cells were washed three times with cytoskeletal TBS buffer (cTBS: 10x stock comprised of 200mM Tris-HCl, 1.54M NaCl, 20mM EGTA, 20mM MgCl2 x 6H2O, pH7.5). Fixed cells were quenched for 10 mins with cTBS containing 50mM NH_4Cl before being blocked and permeabilised for 1 hour at room temperature with cTBS containing 10% BSA, 10% normal goat serum and 0.05% saponin. Cells were then washed once with cTBS. Cells were stained with primary antibodies overnight at 4°C followed by secondary antibodies for 1 hour at room temperature. Antibodies were used at the following dilutions in cTBS with 1% BSA and 0.05% saponin: anti-EDP A2 1:200 (mouse monoclonal sc-365704, Santa Cruz Biotechnology), anti-VASP 1:400 (rabbit polyclonal)[86], anti-Mena 1:400 (rabbit polyclonal)[86], Alexa 488 goat anti-mouse and Alexa568 goat anti-rabbit 1:500 (Invitrogen). Cells were washed three times with cTBS after both primary and secondary antibody incubations. Cells were mounted overnight at room temperature using Prolong Diamond mounting reagents (Invitrogen). Cells were imaged using a CSU-W1 SoRa system (Nikon) with a 60x objective and an intermediate magnification of 2.8x.

Protein expression and purification

BL21-CodonPlus(DE3)-RIL cells were transformed with the plasmid expressing the protein of interest. Single colonies were picked for overnight starter culture growths. Large volume growths were initiated using 25 mL of starter culture per litre of media and grown to an O.D. 600 of ~ 0.7. Cultures were cooled and induced at 18 ˚C overnight with IPTG (0.3 mM for $LPD^{850-1250}$, VASP WT, VASP ∆TD, EVH1 and GST-EDP∆SH3, and 0.6 mM for EDP, SH3, NBAR, and 1 mM for (SH3)5 with EDP A1 linker). Cultures were spun down at 4k rpm at 4 ˚ C, resuspended in a lysis buffer (check specific protein) with 1 mM PMSF. The cell suspension was lysed using a tip sonicator followed by centrifugation at 15k rpm for 1 hour to separate the lysate from insoluble cellular debris. The lysate was filtered with a 0.22 µm syringe filter (Millipore-sigma) prior to affinity chromatography.

The buffers used in the purifications are as follows:

GST lysis buffer: 300 mM NaCl, 50 mM Tris, 2 mM DTT, 1 mM EDTA, pH 8
GST elution buffer: 150 mM NaCl, 50 mM Tris, 2 mM DTT, 1 mM EDTA, 20 mM glutathione, pH 8.
His lysis buffer: 300 mM NaCl, 20 mM Imidazole, 2 mM DTT, pH 8
His elution buffer: 150 mM NaCl, 50 mM Tris, 500 mM Imidazole, 2 mM DTT, pH 8

Cation exchange A buffer (SA): 150 mM NaCl, 20 mM Sodium Phosphate, 1 mM DTT pH 7
Cation exchange B buffer (SB): 1 M NaCl, 20 mM Sodium Phosphate, 1 mM DTT pH 7
Anion exchange A buffer (QA): 150 mM NaCl, 50 mM Tris, 1mM EDTA, 1 mM DTT pH 8
Anion exchange B buffer (QB): 1 M NaCl, 50 mM Tris, 1mM EDTA, 1 mM DTT pH 8
General storage buffer (S buffer): 150 mM NaCl, 20 mM Hepes, 1 mM TCEP, pH 7.4.
VASP storage buffer: 200 mM NaCl, 25 mM Hepes, 1 mM TCEP, 5% glycerol, pH 7.5

LPD$^{850\text{-}1250}$

The lysate was incubated with Ni-NTA agarose beads (Gold Bio) overnight at 4 °C. The beads were washed extensively with the His lysis buffer and incubated with PreScission protease overnight to cleave the GST tag. The beads were further washed with the lysis buffer to remove free GST, and the protein was eluted with the His elution buffer. The eluted protein was buffer exchanged using a HiTrap desalting column into the SA buffer. The protein was further purified using a HiTrap SP HP cation exchange column on a NaCl gradient using the SA and SB buffers. Pure protein fractions were confirmed using SDS-PAGE and were passed on a Superdex S200 pg 16 column (Cytiva) equilibrated with the S buffer.

VASP WT, VASP ΔTD, EVH1

Ecoli expressing the above mentioned VASP constructs were lysed in the GST lysis buffer with 5% glycerol and with PMSF and DNAse. Sepharose 4B glutathione beads were added to the filtered cell lysate and incubated overnight at 4 °C. The beads were washed extensively with the lysis buffer and subsequently incubated with PreScission protease overnight at 4 °C. The beads were spun down and the supernatant containing the protein of interest was isolated. The protein was concentrated and passed on a Superdex S200 column equilibrated with VASP storage buffer. The fractions corresponding to pure VASP were identified using SDS-PAGE.

EDP, SH3, NBAR, GST-EDP, GST-EDP A2, GST-EDP ΔSH3

EDP and its subconstructs were lysed using the GST lysis buffer. The clarified lysate was applied to a GSTrap™FF column (GE Healthcare) and washed extensively with the lysis buffer. The GST tagged protein was eluted using the GST elution buffer containing glutathione. The GST tag was cleaved using PreScission overnight at 4 °C. The GST tag was separated from the protein of interest using an anion exchange chromatography step. The fractions post the ion exchange that contained pure protein was determined using SDS-PAGE and were concentrated and passed on a Superdex S200 pg 16 column (Cytiva) as the final step of the purification. For the GST tagged EDP constructs, the purification after the elution from the GST column continued with the size exclusion chromatography step.

EDP $(SH3)_5$

Lysate is prepared in His lysis buffer. The filtered lysate is passed on a HisTrap column (GE Healthcare). The protein is eluted from the column using the His elution buffer after extensive washing with the lysis buffer. The protein is cleaved off its 6xHis and MBP tag

with TEV protease overnight at 4 ° C. The protein is cleaned up by performing an anion exchange chromatography step with a NaCl gradient generated using the QA and QB buffers. Pure fractions were confirmed using SDS-PAGE, concentrated and passed onto a Superdex S200 column equilibrated in the S buffer.

Actin

Actin was a kind gift from Elizabeth Rhoades. It was purified based on the method described here[87].

Protein labelling

The VASP constructs were labelled N terminally using Alexa Fluor 594 SDP ester. $LPD^{850-1250}$ was labelled using Alexa 647 succinimidyl ester. EDP was labelled using a C5-Maleimide Alexa 594 fluorophore. The labels were added at 7-9-fold excess. The reactions were performed in their respective storage buffer and allowed to occur overnight (16-20 h). The labelled protein was separated from free dye by passing the sample over two serially attached HiTrapTM (5 mL) desalting column.

Protein condensate formation and actin polymerization in the bulk

The experiments were performed in the S buffer with a final salt concentration of 120 mM NaCl, except for EDP and VASP condensates, which were formed without salt adjustments and in the presence of 3% PEG. Given the varying salt contributions from the proteins (refer protein storage buffers), the overall ionic strength was adjusted with 20 mM Hepes pH 7.4 and 1 mM TCEP to obtain the desired final concentration. The protein mixtures were incubated for 10 min at room temperature (21-23 °C) prior to imaging or addition of actin. For fixed time actin polymerization assays, a mixture of unlabelled (4.75 µM) and Rhodamine-green (250 nM) labelled G-actin was added to the condensate mixture and allowed to polymerize for 30 min at room temperature with a final ATP concentration of 25 µM in the solution. The samples were imaged on PEG-PLL passivated chambers.

For generating the size distribution histogram, condensates were first formed in 120 mM NaCl as described above and allowed to incubate for 10 minutes. Actin (5 µM) or G-actin buffer of equal volume was added to the condensates and allowed to evolve for 30 minutes. The samples were deposited on PEG-PLL passivated closed chambers and imaged using confocal microscopy. The size of the condensates and actin rings was measured manually using ImageJ. The data was binned in 0.5 µm intervals.

Actin polymerization in wetted condensates

Glass coverslips were cleaned as described in a previous section. Condensates were prepared and added directly to the coverslip and allowed to settle and wet for 10 minutes. Actin was subsequently added and imaged.

Actin polymerization in tethered condensates

For tethering condensates, clean glass coverslips were functionalised using the following method. PEG-PLL doped with 5% Biotinylated PEG-PLL was added to clean coverslips and allowed to incubate overnight at room temperature in a wet box. The excess polymer was washed thrice with S buffer. Coverslips were treated with 0.02 mg/mL Streptavidin for 15 minutes and washed thrice with S buffer. A mixture consisting of 20 nM Biotin-NTA and 15 μM $NiSO_4$ was preincubated for 30 minutes and added to the coverslips and incubated for 30 minutes. The coverslips were rinsed thrice with S-buffer and were used for experiments.

Condensates were prepared as described earlier and added to the functionalised chamber and allowed to settle for 10 minutes. The condensates tethered themselves to the glass via poly histidine-Ni-NTA interactions. Actin was then added from the top to initiate polymerization.

F-actin staining and actin depolymerization

Alexa647-Phalloidin was used to stain F-actin. It was added at a final concentration of 150 nM at the end of actin polymerization and were allowed to incubate with the sample for 30 min at room temperature. Samples were subsequently imaged.
Latrunculin A was used at a final concentration of 5 μM. It added at the end of actin polymerization and was allowed to incubate with the sample for 30 min at room temperature.

Preparation of supported lipid bilayers (SLB)

Lipid stocks composed of 98:1:1 mol percent DOPC: Ni-NTA DOGS: Marina Blue DHPE lipids were prepared at 5 mg/mL in chloroform. A desired volume of lipids was dried under nitrogen gas and dried further under vacuum between 2 and 16 h. Liposomes were resuspended in S buffer at a concentration of 0.2 mg/mL by vortexing. The suspension was sonicated in a water bath for 30-40 min and subjected to 5 freeze-thaw cycles. The vesicle suspension was finally extruded 13-17 times through a polycarbonate membrane with a pore size of 100 nm. The LUVs were used immediately for preparation of the SLBs.

8 well chambered coverslips (Cellvis) were used for the preparation of SLBs. The wells were first rinsed with 50% (v/v) isopropyl alcohol followed by Milli-Q water. 10 M NaOH was added into the wells for an incubation of 2 h. The wells were thoroughly rinsed with Milli Q water. LUVs were added to the cleaned chambers (150 μL, 0.2 mg/mL) for 30 min. To dislodge unruptured LUVs, the SLBs were rinsed with 650 μL of S buffer thrice. During each rinse, the buffer was repeatedly passed on top of the bilayer without introducing air or scratching the surface, with a minimum volume of 150 μL always maintained in the well. The bilayers were treated with BSA (final concentration 1 mg/mL) for 30 min to

passivate any defects. The wells were rinsed thrice with S buffer and were ready for protein conjugation. The quality of the SLB was verified by performing FRAP.

Coupling proteins to SLBs

Poly histidine tagged $LPD^{850-1250}$ was coupled to SLBs by adding 100 nM total protein (10-20 % labelled protein) to a well. The protein was allowed to bind Ni-NTA functionalised lipids for 15 min, after which unbound protein was removed by gently rinsing the SLBs twice to achieve a 16x dilution. The protein-bilayer system was allowed to relax for 30 min prior to further experiments.

VASP interaction with $LPD^{850-1250}$ coupled SLB and actin polymerization.

VASP (2.5 μM total) was added to the bilayers with the labelled protein concentration of 250 nM. The SLBs were imaged after 30 min of interactions. G-actin (1 μM unlabelled with 100 nM Rhodamine-green labelled) was added at the end of the incubation and images were acquired after 30 min of polymerization.

Correlation analysis

We performed radially averaged normalised auto- and cross-correlation analysis based on a method described elsewhere[20].

GST pull-down assay

Speharose 4B glutathione beads (Cytiva/GE) stored in 20% ethanol were spun down (500-1000 rpm) and washed in water followed by the S buffer. GST tagged protein was coupled to the beads by incubating 25 μM protein with beads at room temperature for 15 min. The beads are spun down and washed twice with the same buffer to ensure removal of uncoupled protein.
The conjugated beads are incubated with mScarlet VASP (and domains) expressing cell lysate or purified VASP or EVH1 (5 μM with 250 nM Alexa Fluor labelled protein) for one hour at room temperature. The beads were washed twice with buffer and imaged.
The fluorescence intensity on the beads were analysed using Image-J. A manual region of interest is drawn on the perimeter of the bead. The integrated intensity in the ROI is corrected for background fluorescence. The fluorescence data plotted in Fig 1 for is normalised by the mean value of the background corrected intensity of the corresponding fluorescent protein pulled down by GST-EDP ΔSH3.

Pyrene actin polymerization assay

Actin polymerization kinetics was assessed by monitoring pyrene labelled actin (Cytoskeleton Cat #AP05) fluorescence. The polymerization was performed in the G-actin buffer (5 mM Tris, pH 8.0 and 0.2 mM CaCl2) supplemented with 0.2 mM ATP and 0.5 mM DTT. The final concentrations used were 2 mM G-Actin with 250 nM pyrene actin, with VASP constructs and $LPD^{850-1250}$ were at 1 μM, EDP and $(SH3)_5$ were used

maintaining the SH3 monomer concentration fixed at 5 μM. Measurements were performed on a Tecan M1000 plate reader.

Giant Unilamellar vesicle experiments

GUVs of lipid composition DOPC/DOPE/marinaBlue-DHPE (69:30:1 mole percent) DOPC/DOPS/DOPE/MarinaBlue-DHPE (24:45:30:1 mole percent) were prepared using electroformation method as described elsewhere[88]. Briefly, 50 μl of the lipid mixture in chloroform (5 mg/ml) was added drop wise onto indium tin oxide (ITO) coated slides and spin coated at 1000 rpm for 1 min. In order to ensure the complete removal of residual solvent, the slides were dried under vacuum for at least 2 h. The lipid films were gently hydrated with aqueous 300 mM sucrose solution and electroformation was carried out at room temperature. An alternating current of amplitude 4 V peak to peak, and frequency 4 Hz was applied across two ITO coated slides for 2 h. The GUVs obtained were stored at room temperature and used after overnight resting.

Experiments involving the recruitment of VASP, polymerization of actin on GUVs and staining with phalloidin was performed as follows. The proteins and small molecules used in the experiment were first diluted in an osmotically balanced buffer (with respect to the sucrose solution used for GUV preparation) after which the GUVs were added to the mixture. The GUVs imaged immediately using a closed coverslip passivated with β-Casein.

References

1 Kaksonen, M. & Roux, A. Mechanisms of clathrin-mediated endocytosis. *Nature reviews Molecular cell biology* **19**, 313-326 (2018).

2 Hemalatha, A. & Mayor, S. Recent advances in clathrin-independent endocytosis. *F1000Research* **8** (2019).

3 Boucrot, E. *et al.* Endophilin marks and controls a clathrin-independent endocytic pathway. *Nature* **517**, 460-465 (2015).

4 Casamento, A. & Boucrot, E. Molecular mechanism of Fast Endophilin-Mediated Endocytosis. *Biochemical Journal* **477**, 2327-2345 (2020).

5 McMahon, H. T. & Boucrot, E. Molecular mechanism and physiological functions of clathrin-mediated endocytosis. *Nature reviews Molecular cell biology* **12**, 517-533 (2011).

6 Chakrabarti, R., Lee, M. & Higgs, H. N. Multiple roles for actin in secretory and endocytic pathways. *Current Biology* **31**, R603-R618 (2021).

7 Hinze, C. & Boucrot, E. Local actin polymerization during endocytic carrier formation. *Biochemical Society Transactions* **46**, 565-576 (2018).

8 Qualmann, B., Kessels, M. M. & Kelly, R. B. Molecular links between endocytosis and the actin cytoskeleton. *The Journal of cell biology* **150**, F111-F116 (2000).

9 Rohatgi, R. *et al.* The interaction between N-WASP and the Arp2/3 complex links Cdc42-dependent signals to actin assembly. *Cell* **97**, 221-231 (1999).

10 Pruyne, D. *et al.* Role of formins in actin assembly: nucleation and barbed-end association. *Science* **297**, 612-615 (2002).

11 Krause, M., Dent, E. W., Bear, J. E., Loureiro, J. J. & Gertler, F. B. Ena/VASP proteins: regulators of the actin cytoskeleton and cell migration. *Annual review of cell and developmental biology* **19**, 541-564 (2003).

12 Hansen, S. D. & Mullins, R. D. Lamellipodin promotes actin assembly by clustering Ena/VASP proteins and tethering them to actin filaments. *Elife* **4**, e06585 (2015).

13 Carman, P. J. & Dominguez, R. BAR domain proteins—a linkage between cellular membranes, signaling pathways, and the actin cytoskeleton. *Biophysical reviews* **10**, 1587-1604 (2018).

14 Vehlow, A. *et al.* Endophilin, Lamellipodin, and Mena cooperate to regulate F-actin-dependent EGF-receptor endocytosis. *The EMBO journal* **32**, 2722-2734 (2013).

15 Lim, K. B. *et al.* The Cdc42 effector IRSp53 generates filopodia by coupling membrane protrusion with actin dynamics. *Journal of Biological Chemistry* **283**, 20454-20472 (2008).

16 Otsuki, M., Itoh, T. & Takenawa, T. Neural Wiskott-Aldrich syndrome protein is recruited to rafts and associates with endophilin A in response to epidermal growth factor. *Journal of Biological Chemistry* **278**, 6461-6469 (2003).

17 Aspenström, P. Formin-binding proteins: modulators of formin-dependent actin polymerization. *Biochimica et Biophysica Acta (BBA)-Molecular Cell Research* **1803**, 174-182 (2010).

18 Rotty, J. D., Wu, C. & Bear, J. E. New insights into the regulation and cellular functions of the ARP2/3 complex. *Nature reviews Molecular cell biology* **14**, 7-12 (2013).

19 Hak, L. C. W. *et al.* FBP17 and CIP4 recruit SHIP2 and lamellipodin to prime the plasma membrane for fast endophilin-mediated endocytosis. *Nature cell biology* **20**, 1023-1031 (2018).
20 Mondal, S. *et al.* Multivalent interactions between molecular components involved in fast endophilin mediated endocytosis drive protein phase separation. *Nature Communications* **13**, 5017 (2022).
21 Ringstad, N., Nemoto, Y. & De Camilli, P. The SH3p4/Sh3p8/SH3p13 protein family: binding partners for synaptojanin and dynamin via a Grb2-like Src homology 3 domain. *Proceedings of the National Academy of Sciences* **94**, 8569-8574 (1997).
22 Renard, H.-F. *et al.* Endophilin-A2 functions in membrane scission in clathrin-independent endocytosis. *Nature* **517**, 493-496 (2015). https://doi.org/10.1038/nature14064
23 Krause, M. *et al.* Lamellipodin, an Ena/VASP ligand, is implicated in the regulation of lamellipodial dynamics. *Developmental cell* **7**, 571-583 (2004).
24 Michael, M., Vehlow, A., Navarro, C. & Krause, M. c-Abl, Lamellipodin, and Ena/VASP proteins cooperate in dorsal ruffling of fibroblasts and axonal morphogenesis. *Current Biology* **20**, 783-791 (2010).
25 Ferron, F., Rebowski, G., Lee, S. H. & Dominguez, R. Structural basis for the recruitment of profilin–actin complexes during filament elongation by Ena/VASP. *The EMBO journal* **26**, 4597-4606 (2007).
26 Gertler, F. B. *et al.* enabled, a dosage-sensitive suppressor of mutations in the Drosophila Abl tyrosine kinase, encodes an Abl substrate with SH3 domain-binding properties. *Genes & Development* **9**, 521-533 (1995).
27 Brühmann, S. *et al.* Distinct VASP tetramers synergize in the processive elongation of individual actin filaments from clustered arrays. *Proceedings of the National Academy of Sciences* **114**, E5815-E5824 (2017).
28 Banjade, S. & Rosen, M. K. Phase transitions of multivalent proteins can promote clustering of membrane receptors. *eLife* **3**, e04123 (2014). https://doi.org/10.7554/eLife.04123
29 Case, L. B., Zhang, X., Ditlev, J. A. & Rosen, M. K. Stoichiometry controls activity of phase-separated clusters of actin signaling proteins. *Science* **363**, 1093-1097 (2019). https://doi.org/10.1126/science.aau6313
30 Alberti, S., Gladfelter, A. & Mittag, T. Considerations and challenges in studying liquid-liquid phase separation and biomolecular condensates. *Cell* **176**, 419-434 (2019).
31 O'Flynn, B. G. & Mittag, T. The role of liquid–liquid phase separation in regulating enzyme activity. *Current opinion in cell biology* **69**, 70-79 (2021).
32 Wiegand, T. & Hyman, A. A. Drops and fibers—how biomolecular condensates and cytoskeletal filaments influence each other. *Emerging topics in life sciences* **4**, 247 (2020).
33 Hernández-Vega, A. *et al.* Local nucleation of microtubule bundles through tubulin concentration into a condensed tau phase. *Cell reports* **20**, 2304-2312 (2017).
34 Cabrales Fontela, Y. *et al.* Multivalent cross-linking of actin filaments and microtubules through the microtubule-associated protein Tau. *Nature communications* **8**, 1981 (2017).
35 Graham, K. *et al.* Liquid-like VASP condensates drive actin polymerization and dynamic bundling. *Nature Physics* **19**, 574-585 (2023).

36 Yu, Y. & Yoshimura, S. H. Self-assembly of CIP4 drives actin-mediated asymmetric pit-closing in clathrin-mediated endocytosis. *Nature Communications* **14**, 4602 (2023).
37 Jonathan Michael, D. *et al.* Biomolecular condensation orchestrates clathrin-mediated endocytosis in plants. *bioRxiv*, 2022.2003.2017.484738 (2023). https://doi.org/10.1101/2022.03.17.484738
38 Day, K. J. *et al.* Liquid-like protein interactions catalyse assembly of endocytic vesicles. *Nature Cell Biology*, 1-11 (2021).
39 Dragwidge, J. M. & Van Damme, D. Protein phase separation in plant membrane biology: more than just a compartmentalization strategy. *The Plant Cell*, koad177 (2023).
40 Bergeron-Sandoval, L.-P. *et al.* Endocytic proteins with prion-like domains form viscoelastic condensates that enable membrane remodeling. *Proceedings of the National Academy of Sciences* **118**, e2113789118 (2021).
41 Ferreira, A. P. A. *et al.* Cdk5 and GSK3β inhibit fast endophilin-mediated endocytosis. *Nature communications* **12**, 1-16 (2021).
42 Disanza, A. *et al.* CDC42 switches IRSp53 from inhibition of actin growth to elongation by clustering of VASP. *The EMBO journal* **32**, 2735-2750 (2013).
43 Rosano, G. L. & Ceccarelli, E. A. Recombinant protein expression in Escherichia coli: advances and challenges. *Frontiers in microbiology* **5**, 172 (2014).
44 Sahdev, S., Khattar, S. K. & Saini, K. S. Production of active eukaryotic proteins through bacterial expression systems: a review of the existing biotechnology strategies. *Molecular and cellular biochemistry* **307**, 249-264 (2008).
45 Pokrant, T. *et al.* Ena/VASP clustering at microspike tips involves lamellipodin but not I-BAR proteins, and absolutely requires unconventional myosin-X. *Proceedings of the National Academy of Sciences* **120**, e2217437120 (2023). https://doi.org/10.1073/pnas.2217437120
46 Faix, J. & Rottner, K. Ena/VASP proteins in cell edge protrusion, migration and adhesion. *Journal of Cell Science* **135**, jcs259226 (2022).
47 Cheng, K. W. & Mullins, R. D. Initiation and disassembly of filopodia tip complexes containing VASP and lamellipodin. *Molecular biology of the cell* **31**, 2021-2034 (2020).
48 Su, X. *et al.* Phase separation of signaling molecules promotes T cell receptor signal transduction. *Science* **352**, 595-599 (2016).
49 Wang, H.-Y. *et al.* Coupling of protein condensates to ordered lipid domains determines functional membrane organization. *Science Advances* **9**, eadf6205 (2023).
50 Shelby, S. A., Castello-Serrano, I., Wisser, K. C., Levental, I. & Veatch, S. L. Membrane phase separation drives responsive assembly of receptor signaling domains. *Nature Chemical Biology* **19**, 750-758 (2023).
51 Brangwynne, C. P. *et al.* Germline P granules are liquid droplets that localize by controlled dissolution/condensation. *Science* **324**, 1729-1732 (2009).
52 Su, Q., Mehta, S. & Zhang, J. Liquid-liquid phase separation: Orchestrating cell signaling through time and space. *Molecular cell* **81**, 4137-4146 (2021).
53 Carlier, M. F., Pantaloni, D. & Korn, E. D. The effects of Mg2+ at the high-affinity and low-affinity sites on the polymerization of actin and associated ATP hydrolysis. *Journal of Biological Chemistry* **261**, 10785-10792 (1986).

54 Agudo-Canalejo, J. *et al.* Wetting regulates autophagy of phase-separated compartments and the cytosol. *Nature* **591**, 142-146 (2021).
55 Mangiarotti, A., Chen, N., Zhao, Z., Lipowsky, R. & Dimova, R. Wetting and complex remodeling of membranes by biomolecular condensates. *Nature Communications* **14**, 2809 (2023).
56 Tsai, F.-C. *et al.* Activated I-BAR IRSp53 clustering controls the formation of VASP-actin–based membrane protrusions. *Science Advances* **8**, eabp8677 (2022).
57 Mattila, P. K. *et al.* Missing-in-metastasis and IRSp53 deform PI(4,5)P2-rich membranes by an inverse BAR domain–like mechanism. *Journal of Cell Biology* **176**, 953-964 (2007). https://doi.org/10.1083/jcb.200609176
58 Leventis, P. A. & Grinstein, S. The distribution and function of phosphatidylserine in cellular membranes. *Annual review of biophysics* **39**, 407-427 (2010).
59 Farsad, K. *et al.* Generation of high curvature membranes mediated by direct endophilin bilayer interactions. *The Journal of cell biology* **155**, 193-200 (2001).
60 Mondal, S., Narayan, K. B., Powers, I., Botterbusch, S. & Baumgart, T. Endophilin recruitment drives membrane curvature generation through coincidence detection of GPCR loop interactions and negative lipid charge. *Journal of Biological Chemistry* **296**, 100140 (2021).
61 Zhu, C., Das, S. L. & Baumgart, T. Nonlinear sorting, curvature generation, and crowding of endophilin N-BAR on tubular membranes. *Biophysical journal* **102**, 1837-1845 (2012).
62 Mim, C. & Unger, V. M. Membrane curvature and its generation by BAR proteins. *Trends in biochemical sciences* **37**, 526-533 (2012).
63 van der Gucht, J. & Sykes, C. Physical model of cellular symmetry breaking. *Cold Spring Harbor perspectives in biology* **1**, a001909 (2009).
64 Abu Shah, E. & Keren, K. Symmetry breaking in reconstituted actin cortices. *Elife* **3**, e01433 (2014).
65 Bray, D. & White, J. G. Cortical flow in animal cells. *Science* **239**, 883-888 (1988).
66 Hirokawa, N., Tanaka, Y. & Okada, Y. Left–right determination: involvement of molecular motor KIF3, cilia, and nodal flow. *Cold Spring Harbor perspectives in biology* **1**, a000802 (2009).
67 Xia, S. *et al.* Nanoscale architecture of the cortical actin cytoskeleton in embryonic stem cells. *Cell reports* **28**, 1251-1267 (2019).
68 Miyazaki, M., Chiba, M., Eguchi, H., Ohki, T. & Ishiwata, S. i. Cell-sized spherical confinement induces the spontaneous formation of contractile actomyosin rings in vitro. *Nature cell biology* **17**, 480-489 (2015).
69 Ledoux, B. *et al.* Plasma membrane nanodeformations promote actin polymerization through CIP4/CDC42 recruitment and regulate type II IFN signaling. *Science Advances* **9**, eade1660 (2023).
70 Fritzsche, M. *et al.* Self-organizing actin patterns shape membrane architecture but not cell mechanics. *Nature communications* **8**, 14347 (2017).
71 Yang, C. *et al.* Actin polymerization promotes invagination of flat clathrin-coated lattices in mammalian cells by pushing at lattice edges. *Nature communications* **13**, 6127 (2022).
72 Ansari, S. *et al.* Active Condensation of Filaments Under Spatial Confinement. *Frontiers in Physics* **10**, 897255 (2022).

73 e Silva, M. S. *et al.* Self-organized patterns of actin filaments in cell-sized confinement. *Soft Matter* **7**, 10631-10641 (2011).
74 Gittes, F., Mickey, B., Nettleton, J. & Howard, J. Flexural rigidity of microtubules and actin filaments measured from thermal fluctuations in shape. *The Journal of cell biology* **120**, 923-934 (1993).
75 Chandrasekaran, A., Graham, K., Stachowiak, J. C. & Rangamani, P. Kinetic trapping organizes actin filaments within liquid-like protein droplets. *Nature Communications* **15**, 3139 (2024).
76 Weirich, K. L., Dasbiswas, K., Witten, T. A., Vaikuntanathan, S. & Gardel, M. L. Self-organizing motors divide active liquid droplets. *Proceedings of the National Academy of Sciences* **116**, 11125-11130 (2019).
77 Yan, V. T., Narayanan, A., Wiegand, T., Jülicher, F. & Grill, S. W. A condensate dynamic instability orchestrates actomyosin cortex activation. *Nature* **609**, 597-604 (2022).
78 Keber, F. C., Nguyen, T., Mariossi, A., Brangwynne, C. P. & Wühr, M. Evidence for widespread cytoplasmic structuring into mesoscale condensates. *Nature cell biology* (2024). https://doi.org/10.1038/s41556-024-01363-5
79 Pyo, A. G. T., Zhang, Y. & Wingreen, N. S. Proximity to criticality predicts surface properties of biomolecular condensates. *Proc Natl Acad Sci U S A* **120**, e2220014120 (2023). https://doi.org/10.1073/pnas.2220014120
80 Tang, Y. *et al.* Identification of the endophilins (SH3p4/p8/p13) as novel binding partners for the β1-adrenergic receptor. *Proceedings of the National Academy of Sciences* **96**, 12559-12564 (1999).
81 Nast-Kolb, T., Bleicher, P., Payr, M. & Bausch, A. R. VASP localization to lipid bilayers induces polymerization driven actin bundle formation. *Molecular Biology of the Cell* **33**, ar91 (2022).
82 Carlsson, A. E. Membrane bending by actin polymerization. *Current opinion in cell biology* **50**, 1-7 (2018).
83 Ma, R. & Berro, J. Crosslinking actin networks produces compressive force. *Cytoskeleton* **76**, 346-354 (2019).
84 Capraro, B. R. *et al.* Kinetics of endophilin N-BAR domain dimerization and membrane interactions. *Journal of Biological Chemistry* **288**, 12533-12543 (2013).
85 Melo, A. M., Elbaum-Garfinkle, S. & Rhoades, E. in *Methods in Cell Biology* Vol. 141 (eds Stuart C. Feinstein & Nichole E. LaPointe) 27-44 (Academic Press, 2017).
86 Bear, J. E. *et al.* Negative regulation of fibroblast motility by Ena/VASP proteins. *Cell* **101**, 717-728 (2000).
87 Spudich, J. A. & Watt, S. The regulation of rabbit skeletal muscle contraction: I. Biochemical studies of the interaction of the tropomyosin-troponin complex with actin and the proteolytic fragments of myosin. *Journal of biological chemistry* **246**, 4866-4871 (1971).
88 Angelova, M. I., Soléau, S., Méléard, P., Faucon, F. & Bothorel, P. Preparation of giant vesicles by external AC electric fields. Kinetics and applications. *Trends in colloid and interface science VI*, 127-131 (1992).